2016

Ultra-wideband antennas

Max Ammann
Technological University Dublin, max.ammann@tudublin.ie

Matthias John
University College Dublin

Giuseppe Ruvio
Technological University Dublin

Recommended Citation

Ammann M.J., John M., Ruvio G. (2016) Ultra-Wideband Antennas. In: Chen Z., Liu D., Nakano H., Qing X., Zwick T. (eds) Handbook of Antenna Technologies. Springer, Singapore. DOI: 10.1007/978-981-4560-44-3_59

Ultra-Wideband Antennas

Max J. Ammann[a]*, Matthias John[b] and Giuseppe Ruvio[c]
[a]School of Electrical and Electronic Engineering, Dublin Institute of Technology, Dublin, Ireland
[b]The Telecommunications Research Centre, (CTVR), Trinity College, University of Dublin, Dublin, Ireland
[c]Antenna & High Frequency Research Centre, Dublin Institute of Technology, Dublin, Ireland

Abstract

The focus of UWB antenna research activity has matured in recent years and currently mainly concentrates on applications such as biomedicine and security. Early UWB antenna designs were driven by the FCC allocation of spectrum in 2002 and focussed on obtaining wide impedance bandwidths with reasonable group delay characteristics. Many of these were simple planar monopoles antennas with canonical geometries. The emergence of new applications channelled the emphasis towards miniaturisation and integration into devices. This required optimisation of the antenna geometries to ensure that good system performance is achieved from the integrated antenna. Many optimisation techniques are available including the spline technique to generate the outline of the antenna element and ground plane. Simple methods based on genetic algorithms are employed and evolutionary algorithms which are capable of optimising for multiple goals are beneficial when multiple antenna parameters are simultaneously investigated. These techniques have proven advantageous especially when time-domain performance is critical and provide solutions for both single-ended and differential feed arrangements. The main applications using UWB channels in the 3.1 GHz – 10.6 GHz spectrum are localization and tracking applications, mainly employing impulse radio UWB imaging, and generally using linear polarization. However circularly-polarized UWB antennas have been developed, both directional and omnidirectional and are being investigated across various systems.

Keywords

Planar monopole antennas; Splines; Optimisation; Time domain performance; Impulse response; Asset tracking antennas; Imaging antennas; Vivaldi antennas; Circular polarisation; Dipole antennas; Miniaturisation; Slot antennas; Radio tags

Introduction

In 1897, Guglielmo Marconi sent the first wireless communication over open sea using a spark-gap transmitter and in 1901, performed the first transatlantic communication from Poldhu, England to St. John's, Newfoundland (Balanis 2005). Because of the spark-gap transmitter, the signal used by Marconi was inherently wideband. Since then the evolution of radio technology has greatly increased. For many of the following decades, radio technology advancements focussed mainly on narrow band transmission, due to the congestion in the electromagnetic spectrum. However in the late 1960's, researchers started to study Ultra Wide Band (UWB) technology. Between 1977 and 1989 the United State Air Force (USAF) had a program on the UWB system (Barret 2001) and some universities focused

---

*Email: max.ammann@dit.ie

on the interaction of short pulses with matter. In 1994 T.E. McEwan invented the Micropower Impulse Radar (MIR) which proved to be the first compact, inexpensive and low power radar, which consumes only microwatts from batteries (Azevedo and McEwan 1996).

In 2002, the Federal Communication Commission (FCC) allocated the 3.1–10.6 GHz for UWB unlicensed use and standardisation began. It limited the maximum Equivalent Isotropic Radiated Power (EIRP) for UWB radio to −41.3 dBm/MHz (74 nW/MHz) and specified that a UWB signal must have, at any point in time, a fractional bandwidth equal to or greater than 20 % or have a 500 MHz bandwidth regardless of the fractional bandwidth (Allen et al. 2007). The high-data rate UWB standard was prepared by the IEEE 802.15.3a task group (Mandke et al. 2003), but ceased in early 2006. However, a high data rate Multi-Band OFDM scheme was standardized by the ECMA-368 standard. In 2004, the IEEE 802.15.4a task group was established for low rate UWB systems which chose to use two approaches for the physical layer, the Direct Sequence UWB (DS-UWB) and the Chirp Spread Spectrum (CSS) (IEEE 2011). The IEEE since published the IEEE 802.15.6 standard for Body-Area-Networks, which provides for UWB channels. Because of their very wide bandwidth, UWB signals have a high temporal resolution (typically less than 1 ns), making this technology particularly suitable for Wireless Sensor Network (WSN) and Real Time Location System (RTLS).

Some of the most popular antennas employed in modern wideband wireless communications systems are the dipole and monopole family. These elements exhibit broad impedance bandwidths which can be extended by increasing the radius of the cylindrical element. This is true up to a point where the stepped radius from the feed probe to the cylindrical element becomes abrupt. Tapering this transition is beneficial and used in wideband elements such as biconical dipoles, but cost limits these to laboratory applications. However, it has been shown that replacing the cylindrical element of a monopole or dipole with planar elements provide a wider impedance bandwidth, and with some simple adjustment, UWB bandwidth. The first mention of the planar monopole antenna was in a textbook in 1968 by Meinke and Gundlach (1968), who describe it as a variant of the cylindrical and conical monopole. Dubost and Zisler provided more detail about the wide impedance characteristics of this antenna in 1976 (Dubost and Zisler 1976). A disc-shaped planar monopole antenna was subsequently reported in 1991 by Honda et al. (1992), who proposed this antenna for the Japanese television band (90–770 MHz). In 1992 he reported one which had a 10 dB impedance bandwidth ratio in excess of 10:1 (Honda et al. 1991). A model for determining the value of the input impedance of the circular disc-shaped monopole was reported in 1993 by Hammoud et al. (1993) based on the Method of Moments. Circular and elliptical disc monopoles were also studied in 1998 by Agrawall et al. (1998), who proposed a formula for predicting the frequency corresponding to the lower edge of the impedance bandwidth. Since then a plethora of canonical shapes were reported to provide UWB impedance bandwidth. These include square, rectangular, elliptical, circular, trapezoidal and triangular (Ammann 1999; Evans and Ammann 1999). The use of triangular and bow-tie geometries for the planar element were also investigated by Chen (2000). Furthermore, bevelling of the shapes and feed asymmetry was introduced to further widen the impedance bandwidths and very wide impedance bandwidth ratios were realised (Ammann 2001; Ammann and Chen 2003a, b).

At the time, these elements were studied when placed above a classical ground plane and in many cases, only the impedance properties were reported. As time moved on, many of the geometries migrated to printed antennas geometries where the ground planes are printed on the same PCB (Kuo and Wong 2002; Go and Jung 2004; Liang et al. 2004). The ground planes, which were often excluded from any design rules, were populated with components and modules, which is particularly attractive for portable terminal devices (Fig. 1).

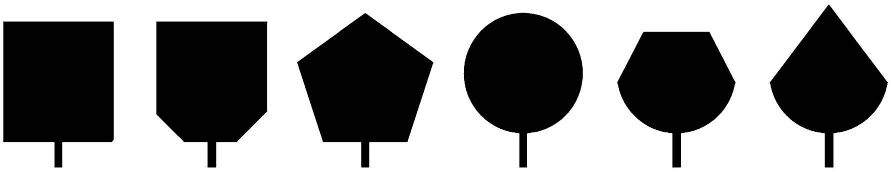

Fig. 1 A selection of planar monopole shapes including square, tapered square, pentagonal, circular and combinations of these

Optimised UWB Antennas

Geometries of recent UWB antennas are based on simple geometric elements, such as rectangles (Chen et al. 2006a), circles (Liang et al. 2005) or ellipsis (Angelopoulos et al. 2006), or a combination of these (Griffiths et al. 2005). Examples for combining multiple elements are a combination of rectangles, triangles and circles in (Karacolak and Topsakal 2006) or polygons, circles and exponential curves in (Chen et al. 2006b).

To optimise a specific antenna design, a number of optimisation methods are available ranging from simple interpolation methods to evolutionary algorithms capable of optimising for multiple goals. There is a large number of publications available dealing with electromagnetic optimisation. Evolutionary methods include genetic algorithm (GA) (Johnson and Rahmat-Samii 1997; Haupt 2007; John and Ammann 2007) and particle swarm optimisation (PSO) (Jin and Rahmat-Samii 2005; Donelli and Massa 2005). Today, a variety of methods are available in commercial EM software such as CST, Feko or HFSS. In the following example the GA in CST Microwave Studio is used.

This section analyses antenna geometries based on quadratic Bézier spline curves (Foley et al. 1993; Bartels et al. 1996). Splines are curves generated by quadratic interpolation between control points. This spline is used to outline the radiating element and/or ground plane of an antenna. The benefit of this technique is an inherently rounded shape of the radiating element and a straight forward way of assigning parameters to the control points. The design methodology overcomes the geometrical constraints of a circular or elliptical disk and the need of combining simple geometric elements.

Spline Theory

A spline is a function defined by polynomials. In mathematics, splines are used for interpolation and smoothing problems. In computer graphics, the term spline refers to a piecewise polynomial parametric curve used to illustrate complex shapes (Bartels et al. 1996). Splines are classified by the degree of the polynomial, such as linear, quadratic, cubic or higher order splines. In computer graphics and CAD programs, quadratic and cubic splines are most common (Foley et al. 1993). Bézier curves are named after Dr. Pierre Bézier who used these curves to design automobile bodies for Renault in the 1960s.

The electromagnetic simulator CST Microwave Studio (MWS) uses the quadratic form of these curves. One curve segment of a quadratic Bézier spline is the path traced by the function B(t)

$$B(t) = (1-t)^2 P_0 + 2t(1-t)P_1 + t^2 P_2; t \in [0,1], \tag{1}$$

when t is swept from 0 to 1. The points P_n are defined by their x- and y-coordinates in a two dimensional plane.

Figure 2 shows this path for various *t*. It can be seen that, as *t* is varied in five steps from 0 to 1, the '×' (green) traces a quadratic curve (red). To create more complex shapes, an arbitrary number of Bézier curves can be attached together in a chain.

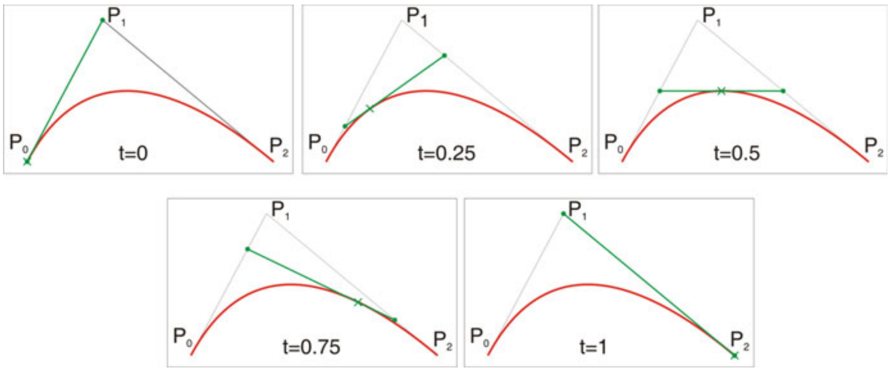

Fig. 2 Quadratic Bézier curve for various t

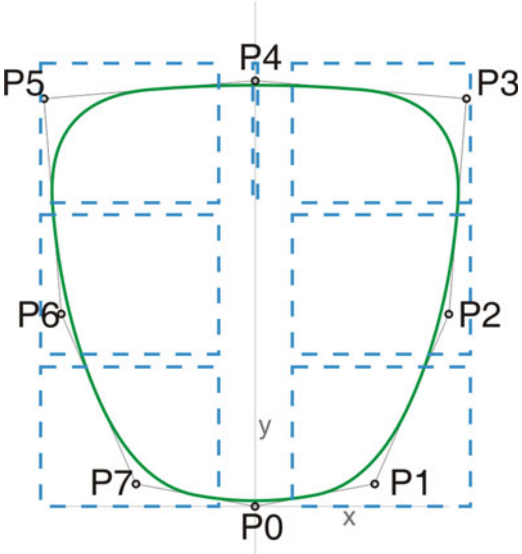

Fig. 3 Control points and bounds for spline geometry

Example of a Spline Based Antenna Geometry

As an example a quadratic Bézier spline is used to describe the outline of the radiating element of a printed monopole antenna in the following way. The spline curve is defined by 8 control points P0–P7. Figure 3 shows the outline curve and its control points. Point P0 is fixed at (0,0), this is where the antenna is fed by a 50 Ω microstrip line. Points P1–P3 are defined their by x and y-coordinates, which are variable parameters. Point P4 is fixed at $y = 0$ and can only be moved along the x-axis. Points P5–P7 are derived from points P1–P3 by mirroring them along the x-axis. In order to achieve a closed curve, the curve ends again in point P0. This creates a symmetrical radiator with the intention of achieving an omnidirectional radiation pattern. The resulting curve can be used as the outline of a radiating element of a printed monopole antenna. It is placed on the substrate with a partial ground plane on the rear, the enclosed area filled with copper and connected to a microstrip feedline.

The coordinates of the control points are used as parameters for optimisation by the genetic algorithm in the CST Studio Suite. Bounds are defined for the coordinates of each point, they are shown in Fig. 3 by blue rectangles. These bounds serve two purposes. Firstly, they constrain the size of the design to be

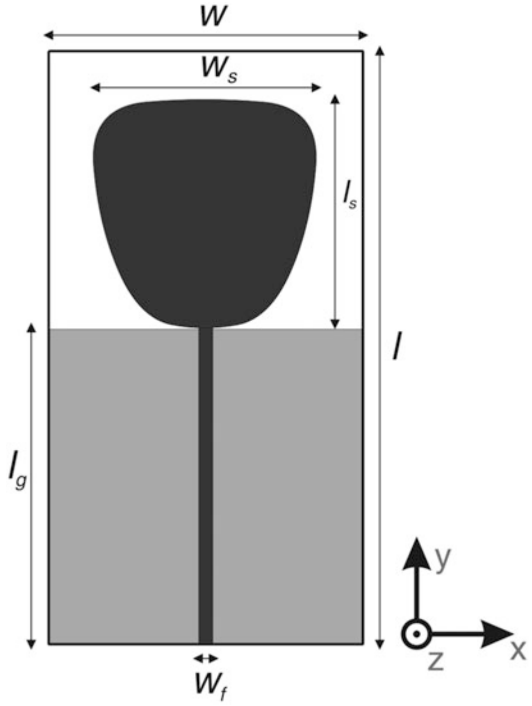

Fig. 4 Geometry of the optimised spline based monopole

within the limits defined by the substrate size. This ensures that the radiating patch does not extend over the side of the substrate. Secondly, the bounds ensure that the resulting spline does not form a loop.

Due to the wide operating bandwidth anticipated from this design, Rogers RO4350B was used as the RF substrate. The substrate size was $w = 45$ mm and $l = 85$ mm with the 45 mm square ground plane located on the rear side. A 2.4 mm wide 50 Ω microstrip feedline is used to feed the antenna. The complete geometry is shown in Fig. 4. It is the result of a GA optimisation with a population size of 30 which was evolved over 20 generations. The fitness function was set to maximise the −10 dB S11 bandwidth within the 0–20 GHz simulation bandwidth. In the resulting geometry, it can be seen that the radiating element curves smoothly away from the feedpoint. The maximal possible height is exploited as point P4 is placed at the maximum of its bound. The dimensions of the spline based radiating element are $l_s = 33$ mm by $w_s = 32$ mm.

Bandwidth

The simulated and measured S11 are shown in Fig. 5. It can be seen that the measured S11 is better than −10 dB from 1.44 GHz to 14.7 GHz. This corresponds to an impedance bandwidth ratio of 10.2:1, which is very wide for a printed monopole.

Surface Currents

The surface currents in the metallised parts of the antenna have been computed for various frequencies. They are show in Fig. 6. For the lowest frequency of 2 GHz (Fig. 6a), the plot indicates a first order resonance. Animation of a series of plots at this frequency for different phases shows that this mode has a standing wave current pattern. Higher modes at 8 GHz or 16 GHz (Fig. 6c and d) show more complex current patterns. An animation of these plots in a phase sweep shows that the current is travelling along the edge of the radiating element. It is concluded that this antenna is working in a hybrid mode (Chen 2007) of operation between a standing wave and a travelling wave antenna.

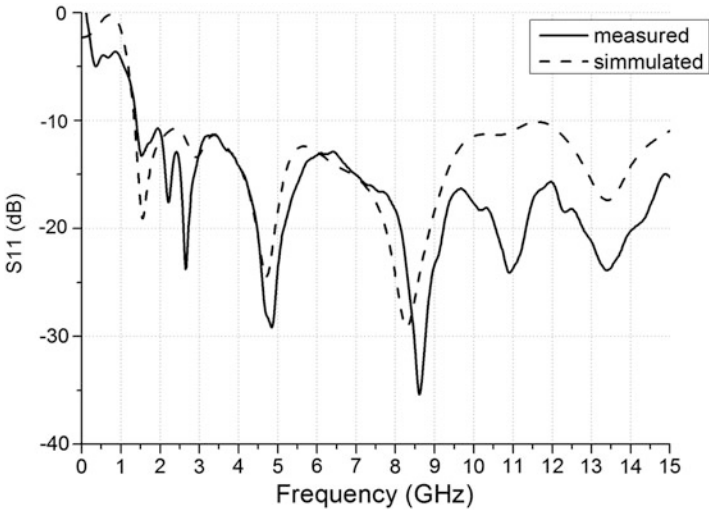

Fig. 5 Simulated and measured S11 of the spline based monopole

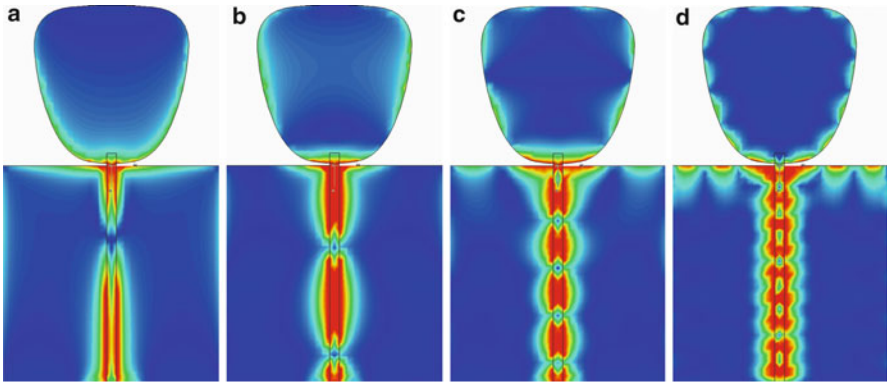

Fig. 6 surface current in the spline based monopole at 2, 4, 8, and 16 GHz

Radiation Pattern

The measured radiation patterns are shown in Fig. 7. The H-plane patterns are found to be omnidirectional up to about 8 GHz. The measured gain is 2.8 dBi at 2 GHz, 4.3 dBi at 6 GHz, 4.8 dBi at 10 GHz and 5.3 dBi at 14 GHz. The simulated radiation efficiency at these frequencies is 91, 96, 92 and 89 % respectively.

Group Delay

Group delay was measured in three orientations of the antennas, front-front, front-side and side-side. Measurement results are shown in Fig. 8. In the UWB band from 3.1 GHz to 10.6 GHz, the group delay variation is below 0.5 ns. Group delay is the derivative of the pulse response of the S21 between the two antennas. A linear phase response is required for low group delay variation. There was no explicit optimisation goal for a linear phase response in this example. A linear phase response is inherent in the spline geometry as the current path is very smooth around the outside of the radiating element. Hence the spline based design methodology is suitable for designing antennas for communication applications where low pulse distortion is required.

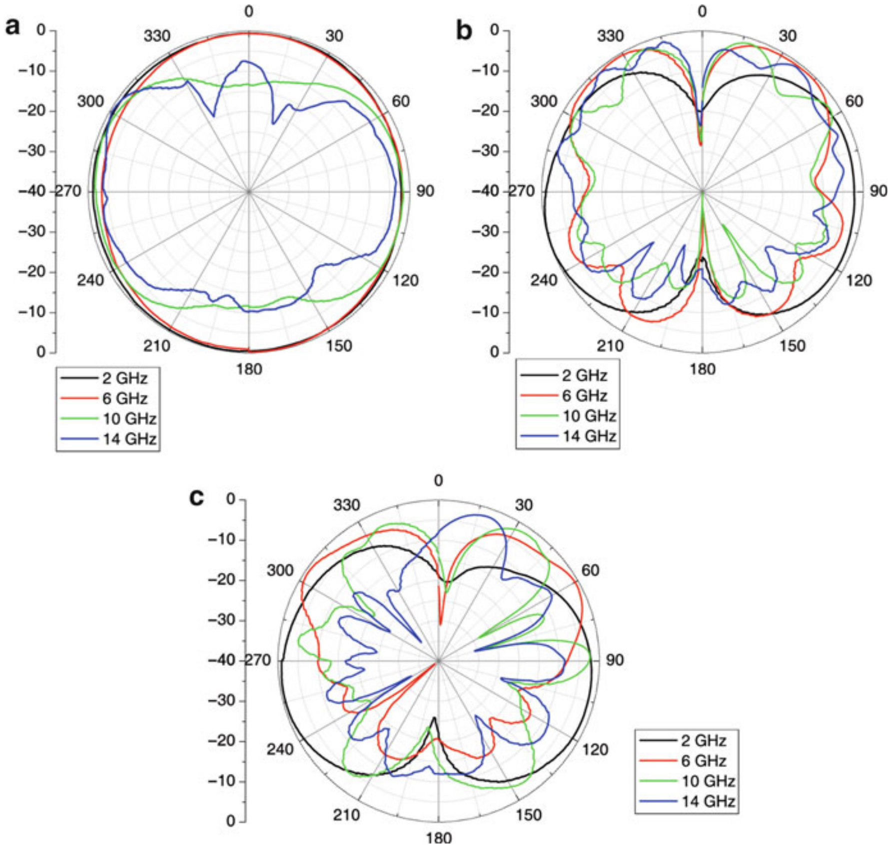

Fig. 7 Measured radiation patterns for the spline based monopole antenna in x-z, x-y and y-z planes

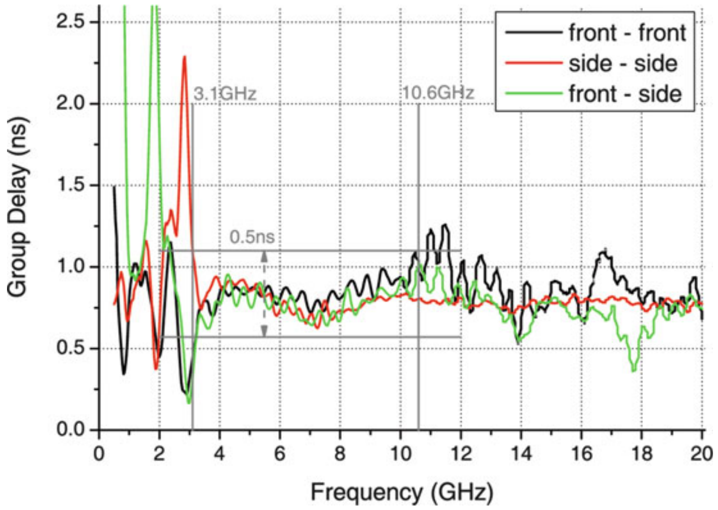

Fig. 8 Measured group delay for a pair of spline based monopole antennas in three orientations

This spline based optimisation technique can be easily adopted to design antennas of constrained size. Figure 9 shows a 40 × 30 mm monopole operating in the 3.1–10.6 GHz band with the ground plane shape also optimised (John and Ammann 2009).

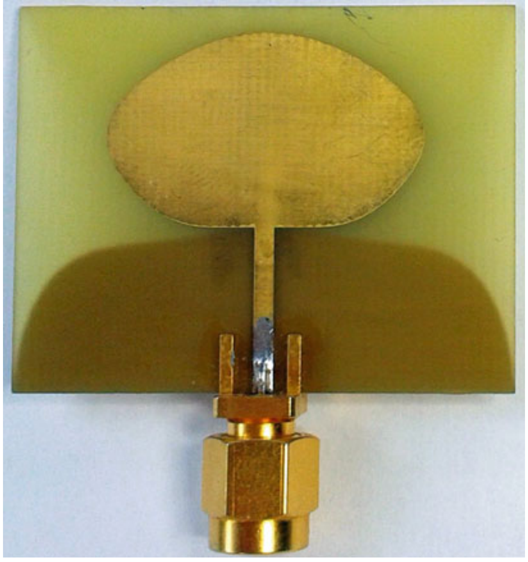

Fig. 9 Small UWB antenna developed at the Dublin Institute of Technology

UWB Antennas Optimised for Time Domain Applications

Impulse radio Ultra Wide Band (IR-UWB) systems use very short pulses (typically less than 1 ns) to achieve very broad bandwidth for low powered communications. The short pulses can be used for UWB Real Time Location System (RTLS) for proximity ranging or localization with centimeter precision. Earlier publications consider and analyse time domain performance of UWB antennas (Schantz and Fullerton 2001; Kwon 2006), but do not optimize for it. Schantz, in (2004) gives general rules on how to minimize dispersion in UWB antennas. Recent publications synthesize UWB antennas from a time-domain perspective by optimizing antenna geometries depending on the pulse shape they radiate (Telzhensky and Leviatan 2006; Dumoulin et al. 2012; Lizzi et al. 2012).

UWB Pulse Shapes

UWB antenna literature predominantly reports Gaussian and Rayleigh pulses, and their derivatives, for antenna excitation (Chen et al. 2004; Lizzi et al. 2009; Chen et al. 2005; Guo et al. 2007). Their characteristics include very low level side lobes in the frequency-domain and fast energy damping in the time-domain. However, the energy distribution across the frequency range is typically bell-shaped and antennas that are optimized with these pulse profiles do not have the bandwidth for an efficient fit to the 802.15.4a spectrum mask (Chen et al. 2005), (Chamaani et al. 2011), (Cerny and Mazanek 2007). While a series of modulated Gaussian pulses can be sequenced (IEEE 2007) to cover the entire UWB mask, the approach increases the duration of the excitation pulse. It extends antenna simulation run-times and adds complexity to the time-domain analysis of the models.

Alternatively, an SRRC pulse overcomes the limitations. The analytical form of the SRRC pulse is shown in Eq.2 (Zhang et al. 2003).

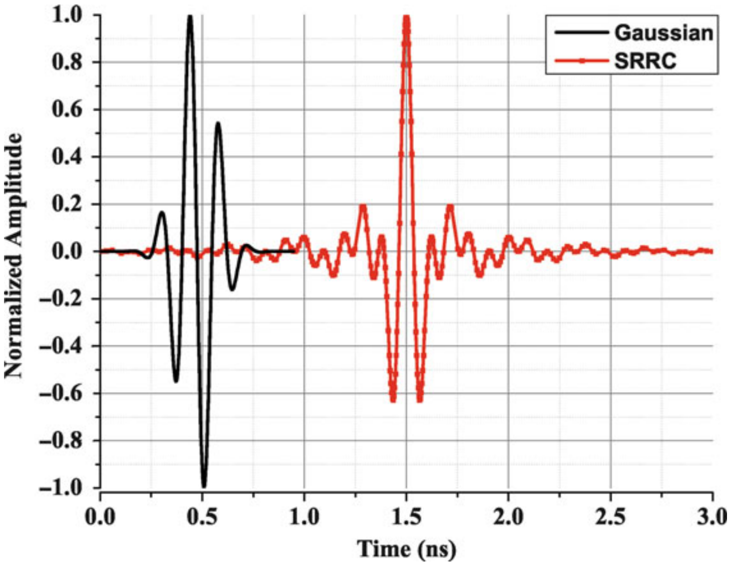

Fig. 10 Modulated Gaussian and Square Root Raised Cosine pulses with respective peak values normalized to unity

$$F_{SRRC}(t) = \left[\frac{2\beta}{\pi\sqrt{T_s}} \times \frac{\cos\left[(1+\beta)\pi \frac{t}{T_s}\right] + \dfrac{\sin\left[(1-\beta)\pi \frac{t}{T_s}\right]}{4\beta \frac{t}{T_s}}}{\left[1 - \left(4\beta \frac{t}{T_s}\right)^2\right]} \right] \tag{2}$$

where t is the time, $T_S = 1/R_S$, R_S being the symbol rate and β is a dimensionless roll-off factor for bandwidth control.

Figure 10 shows an amplitude modulated Gaussian pulse and an amplitude modulated SRRC pulse (roll-off factor of 0.1 and symbol rate of 7.1 GHz); both centred at 6.85 GHz and with the respective peak values normalized to unity. Figure 11 shows the corresponding Power Spectrum Density (PSD) plots with the 802.11.4a UWB indoor use spectrum mask.

The evenly contoured power spectrum of the SRRC pulse, compared to that of the Gaussian pulse, conveys a broader bandwidth at a higher energy level. Although many UWB systems only operate using channels with bandwidths in range 500–1300 MHz, different channels can be used in different jurisdictions and hence it is beneficial to optimise over the full UWB range. The design goal is to create antennas that can support pulses of increased bandwidths across the spectrum profile of the SRRC.

Differentially Fed UWB Antennas

While monopole antennas are suitable for most applications, they need a balanced to unbalanced transformer (BALUN), when connected to a differential IC output. The introduction of the balun incurs losses and dispersion in both transmission and reception mode, impairing the accuracy and range of the overall system. Balanced antennas, such as dipoles or slot antennas can be differentially fed making their integration into the system more straightforward.

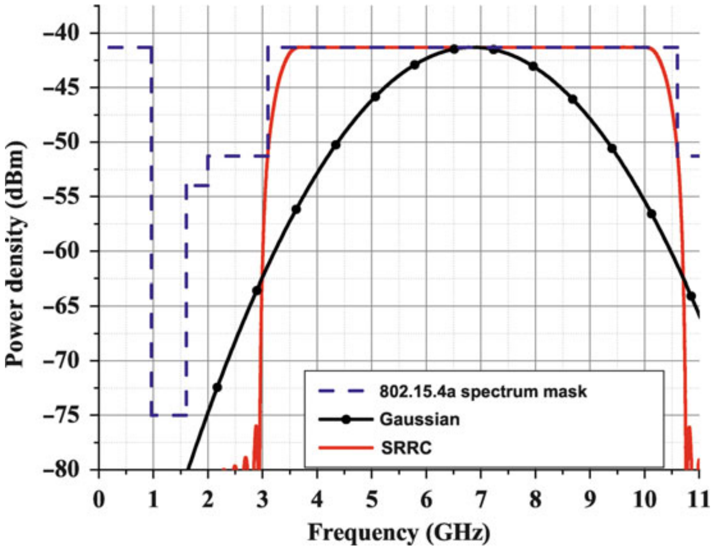

Fig. 11 802.15.4a indoor use spectrum mask with power spectrum density of Gaussian and SRRC pulses; respective peak values normalized to −41.3 dBm

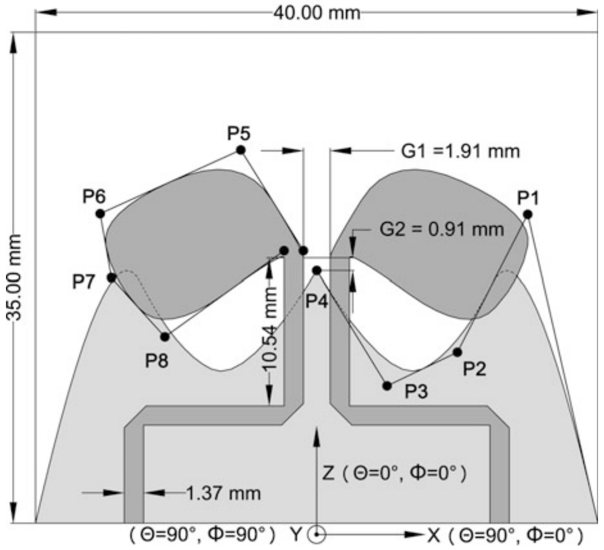

Fig. 12 Gaussian Dipole (GD) geometry

In this example a differentially fed balanced dipole is examined. The dipole geometry is optimised using both a SRRC excitation and a modulated Gaussian like excitation signal. Spectral and time-domain performances of the resulting antennas are compared.

The dipole antennas were optimised for wide-band performance and pulse fidelity, using a SRRC excitation signal for the SRRC dipole (SD) and a modulated Gaussian like excitation signal for the Gaussian dipole (GD) shown in Figs. 10 and 11. Antennas GD and SD, shown in Figs. 12 and 13, are planar dipole-like with a balanced microstrip feed arrangement which requires a small ground plane. They consist of two identical dipole arms (defined by 4 spline points) fed with 50 Ω dual mitred microstrip lines and a mirrored splined ground plane (4 points). The spline points for the radiators have two degrees of

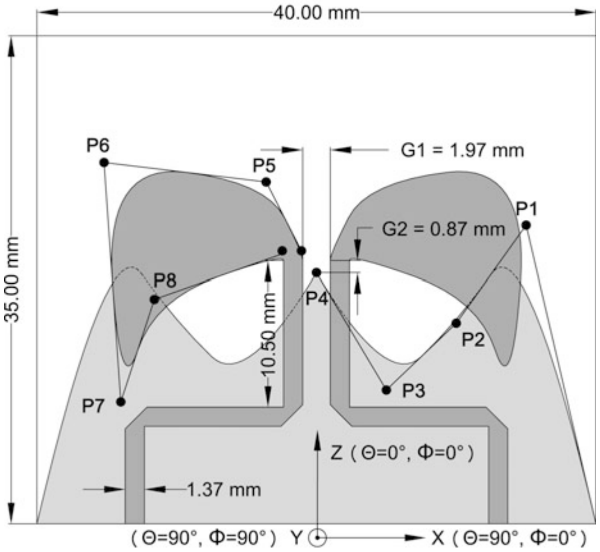

Fig. 13 SRRC Dipole (SD) geometry

freedom (X and Z-axis), while the spline points for the ground plane are restricted to one degree of freedom (Z-axis) in order to limit the complexity of the problem.

Both antennas were fabricated on a 40 × 40 × 0.7 mm FR4 double-sided laminate with a dielectric constant $\varepsilon_r = 4.3$ and loss tangent = 0.02. The antennas were initially performance-optimized without SMA connectors but the simulation model included the connectors to allow a fair comparison between measurement and simulation. The dimensional constraints of the antenna, defined in millimetres, are shown below.

- $P_{1,2,3,4}\ (z) = 5 < z < 26$
- $P_5\ (x) = 0 < x < 4$
- $P_5\ (z) = P_4 < z < 40$
- $P_{6,7,8}\ (x) = 10 < x < 20$
- $P_{6,7,8}\ (z) = P_5 < z < 40$
- $G_1 = 1 < x < 5$
- $G_2 = 0 < z < 5$

Optimisation

The antennas were optimised for best fidelity factor between the excitation signal derivative and the radiated signal. For time-domain optimization, E-field-probes were located 30 cm from the dipoles in the azimuth plane. Simulation time was halved by using field symmetry in the H-plane and by limiting probes to [$\varphi = 90°$, $-90° \leq \theta \leq 90°$ in 5° steps].

A weighted cost function was post-processed for the design iterations using Eq.3.

$$Cost = -0.3 \times \frac{\Gamma}{\alpha} - 0.7 \times \frac{\sum FF}{\gamma}, \text{for } \Gamma < \alpha \tag{3}$$

$$Cost = -0.3 - \left(0.7 \times \frac{\sum FF}{\gamma}\right), \text{for } \Gamma \geq \alpha$$

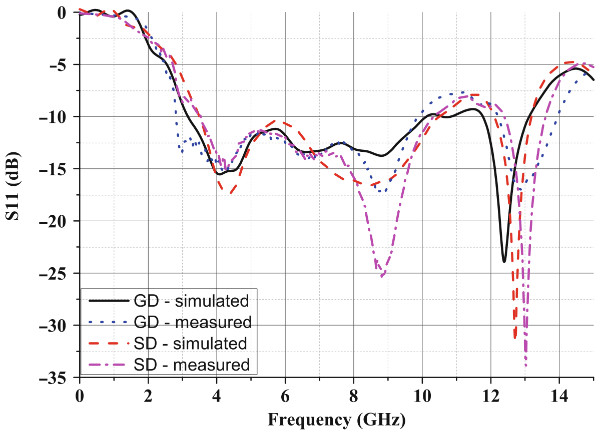

Fig. 14 Simulated and measure S11 for the GD and SD dipoles

where Γ is the least matched magnitude in the S11, α is the S11 match target, *FF* is the fidelity factor (Chen et al. 2005) (field probes relative to the derivative of the excitation pulse) at each angle and γ is the number of FF values. The empirically selected coefficient weightings were chosen to provide a balance between optimization time and accuracy.

Additionally, a subroutine was used to skip simulations of non-realistic structures or re-simulation of identical structures (Guo et al. 2007), more of which occur as the algorithm converges on the optimum range of possible solutions. These significantly reduce the optimization time with minimum effect on the GA behavior. The algorithm also uses an intermediate crossover, the roulette wheel selection, and stops after 30 population iterations (maximum antenna simulations $\leq$ 8085).

Frequency-Domain Results

The simulated and measured S11 for the two Dipoles *GD* and *SD* are illustrated in Fig. 14. The dipoles exhibit an 8 dB return loss across 2.75–10.6 GHz and 2.9–13.8 GHz, respectively. The antennas have good impedance matching for the 3.1–10.7 GHz band, with good agreement between simulations and measurements.

The dipole radiation patterns were similarly measured in the H-plane (Z-Y plane). Figures 15 and 16 show good stability in the radiation pattern across 3.1–10.6 GHz. The dipoles achieve an average realized gain of -0.27 dBi (std. dev. = 2.45) and 0.8 dBi (std. dev. = 2.47) respectively. *Dipole GD* has a maximum gain of 6.4 dBi (θ, $\varphi = 90°, 55°$) at 8.88 GHz, while *Dipole SD* has a maximum gain of 6.87 dBi (θ, $\varphi = 90°, 60°$) at 9.4 GHz.

Time Domain Measurement and Results

To quantify the time-domain performance of an antenna, or a system of two antennas, the most common metric is the Fidelity Factor (FF). The FF is established by the maximum absolute value of the cross-correlation coefficient of the two normalized pulses. It is a useful measure of how much time-domain dispersion an antenna will add to a pulse being transmitted through it.

The antenna and its operating mode determine if the radiated pulse will be radically different to the source pulse. It has been shown that the transient response of an antenna in transmitting mode is proportional to the time derivative of the impulse response of the same antenna in receiving mode (Kanda 1986; Ghosh et al. 2006; Rambabu et al. 2009). Researchers have demonstrated that radiation of UWB pulses involve fields that are time-delayed time-derivatives of the signal currents from the various parts of the transmitting antenna (Siwiak and McKeown 2004). Hence, the simulated radiated pulses have to be cross-correlated with the 1st-order derivative of the excitation pulse.

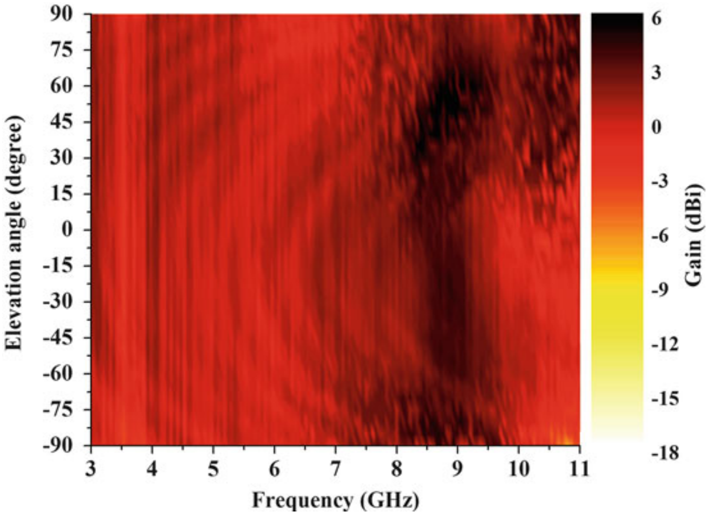

Fig. 15 Measured Dipole GD radiation pattern in the φ = 90° plane

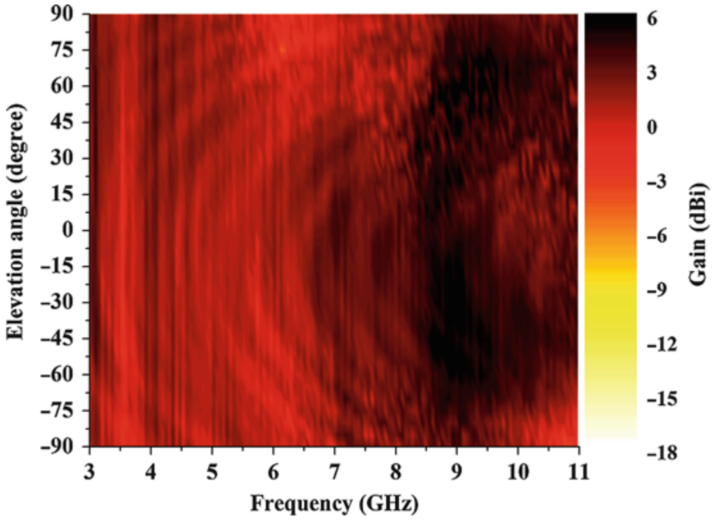

Fig. 16 Measured Dipole SD radiation pattern in the φ = 90° plane

Measurement Setup To generate the SRRC UWB pulse, a digital sampled waveform was exported to a Tektronix AWG 7122C Arbitrary Waveform Generator (AWG). Due to its output voltage limitation, the AWG output signal was amplified with a Picosecond Pulse Labs wideband amplifier (Model 5865) and fed to the antenna under test. Also, in order to accurately measure the radiated pulse, the receiving antenna should not be dispersive. Consequently a directional tapered slot antenna was designed and its geometry is shown in Fig. 17. Using the SRRC pulse (see Fig. 10) as an incident signal instead of excitation signal, it was optimised for optimal time-domain performance on bore-sight in receiving mode. In this operating mode, the antenna has a simulated pulse fidelity factor of 98.6 % at the bore-sight. This result indicates that the received signal at the antenna's port is nearly identical to the replica of the incident signal.

A distance of 20 cm was chosen between the transmitting and receiving antenna to maintain the farfield measurement while achieving an adequate signal to noise ratio (SNR) because from a distance of 50 cm, the SNR dropped to an unacceptable level, impairing the time-domain measurement. Figure 18, depicts the time-domain measurement setup.

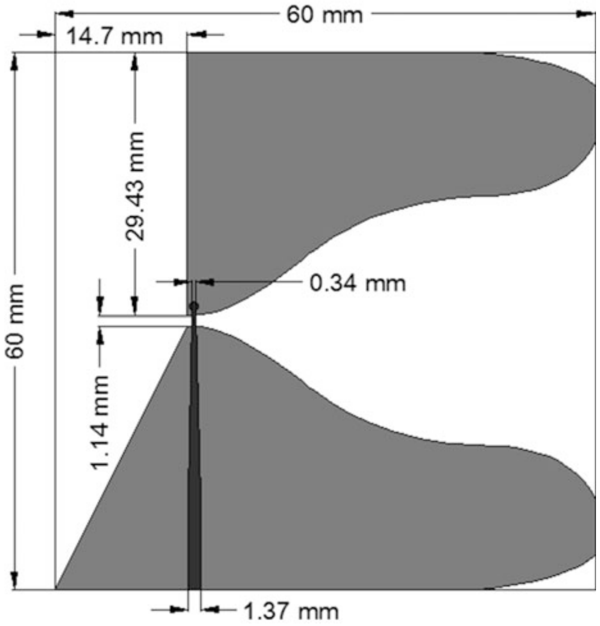

Fig. 17 Tapered slot antenna optimised for time-domain performance in receiving mode

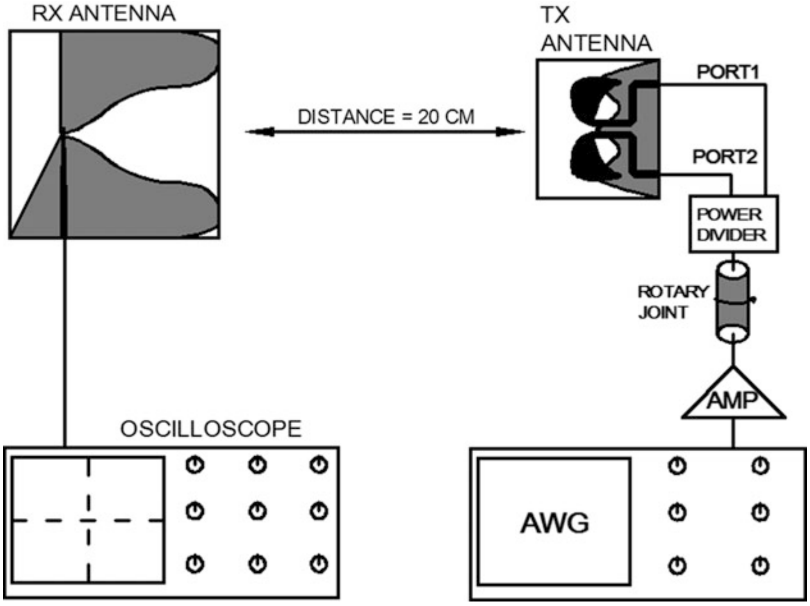

Fig. 18 Time-domain measurement setup

Pulse Equalisation

Because of the imperfect impulse response of the transmit network components, the AWG generated SRRC pulse fed at the AUT's input port suffers from impaired frequency- and time-domain characteristics. If such a signal is fed to the transmit antenna, the measured pulse fidelity will not represent the full transient performance of the AUT.

Figure 19 illustrates the AWG input waveform *in(t)* with the pulse *out(t)* offered to the transmit antenna. To subdue the component losses, the input signal was compensated using Eq.4, where the Inverse Fast

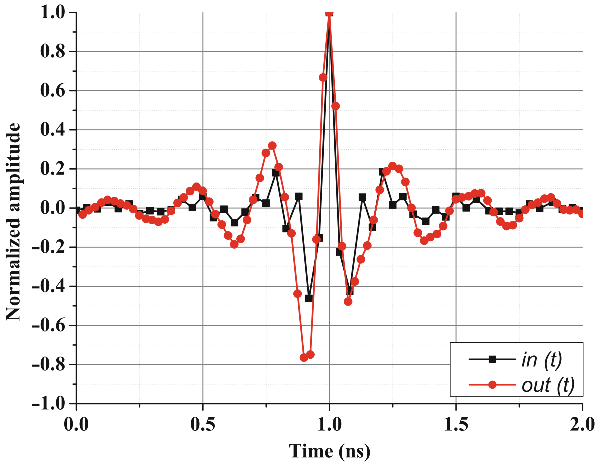

Fig. 19 *in(t)* waveform to AWG and *out(t)* pulse

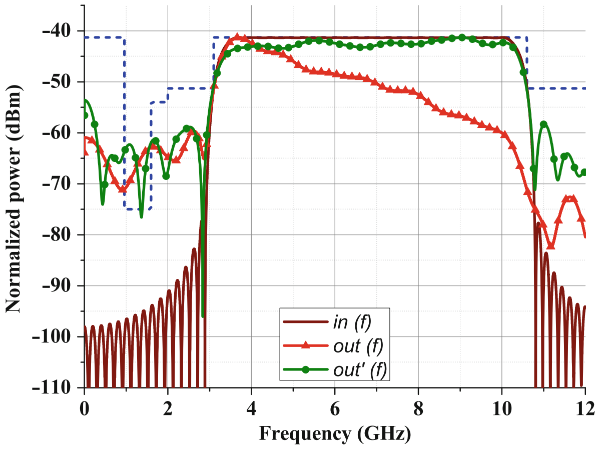

Fig. 20 Input, output and output equalized pulse Power Spectrum

Fourier Transform (IFFT) and the Fast Fourier Transform (FFT) are used to manipulate the pulse in frequency- and time-domain. In Fig. 20, the power spectrum density of the compensated signal *out'(t)*, the input signal *in(t)* and the initial output signal *out(t)* are shown.

$$in'(t) \ = \ IFFT\ [FFT(in(t))\ /\ FFT(out(t))] \tag{4}$$

Compared to the original SRRC signal *in(t)*, the compensated signal *out'(t)* energy distribution level share many characteristics in the UWB band, demonstrating that the transmit network impulse response was equalised. Hence, the *out'(t)* signal was fed at the transmitting antenna port allowing an accurate time-domain characterisation of the AUT.

Antenna Impulse Response De-embedding

In the last section, an equalisation method was presented, suppressing the transmit network impulse response from the measurement. However, in order to get an accurate measure of the radiated signal, the receive network impulse response, which includes the one from the receiving antenna, should also be removed.

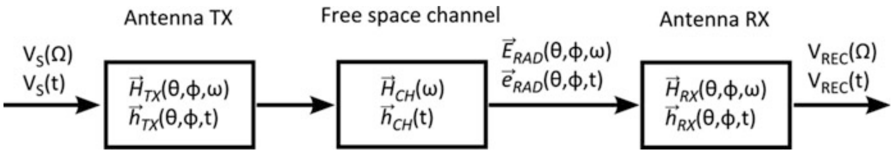

Fig. 21 UWB channel model

Using two identical antennas, in an antenna system configuration, and by using the method described by (Duroc et al. 2007), it is possible to estimate the transient and frequency response of the AUT. Indeed, the UWB channel model can be decomposed in three different blocks, consisting of the transmitting antenna, the free space channel, and the receiving antenna. Each block can be described by a transfer function such as, $\vec{H}_{TX}(\theta,\varphi,\omega), H_{CH}(\ \Omega)$and $\vec{H}_{RX}(\theta,\varphi,\omega)$, as shown on Fig. 21.

Hence the UWB channel can be completely described in both frequency- and time-domain as shown in Eqs.5 and 6 (Kanda 1986).

$$\frac{V_{REC}\ (\omega)}{V_S\ (\omega)} = \vec{H}_{TX}(\theta,\varphi,\omega) \times H_{CH}(\omega)\ \times\ \vec{H}_{RX}(\theta,\varphi,\omega) \tag{5}$$

$$V_{REC}(t) = \vec{h}_{TX}(\theta,\varphi,t) * h_{CH}(t)\ *\ \vec{h}_{RX}(\theta,\varphi,t) * V_S(t) \tag{6}$$

where Ω is the angular frequency, and the symbol $*$ is the convolution symbol. The free space channel transfer function can be defined using Eq.7, where c is the speed of light in free space, d is the antenna separation and λ is the wavelength.

$$H_{CH}(\omega) = \frac{\lambda}{2d}\exp\left(-j\omega\frac{d}{c}\right) \tag{7}$$

Then, by measuring the vectorial S21 of two identical antennas with same orientation, it is possible to deduce the transfer function of the antenna in transmitting and receiving mode as shown in Eqs. 8 and 9.

$$\vec{H}_{TX}(\theta,\varphi,\omega) = \sqrt{\left(\frac{\vec{S}_{21}\ (\theta,\varphi,\omega)}{H_{CH}(\omega)}\frac{j}{\lambda}\right)} \tag{8}$$

$$\vec{H}_{RX}(\theta,\varphi,\omega) = \sqrt{\left(\frac{\vec{S}_{21}\ (\theta,\varphi,\omega)}{H_{CH}(\omega)}\frac{\lambda}{j}\right)} \tag{9}$$

By knowing the transfer function of the receiving antenna, the free space channel and the antenna system's S_{21}, the transfer function of the unknown transmitting antenna can be calculated has shown on Eq.10.

$$\vec{H}_{TX}\ (\theta,\varphi,\omega) = \frac{\vec{S}_{21}(\theta,\varphi,\omega)}{H_{CH}(\omega)\ \times\ \vec{H}_{RX}(\theta,\varphi,\omega)} \tag{10}$$

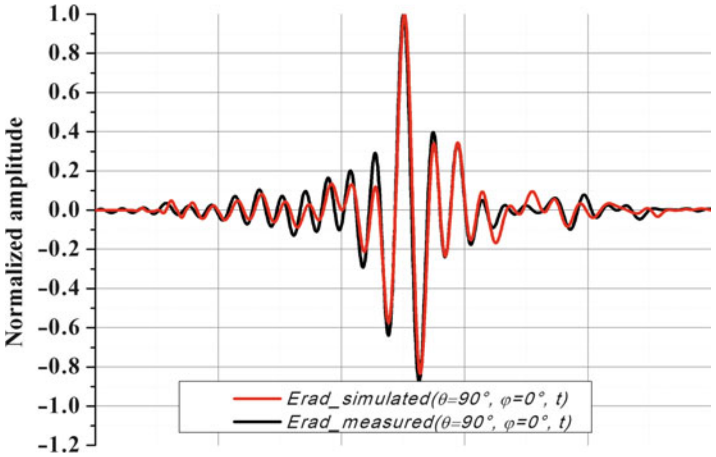

Fig. 22 Simulated and measured radiated pulse

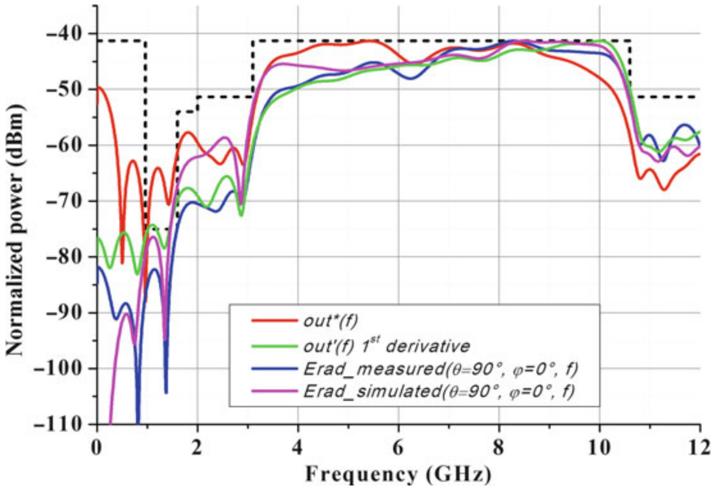

Fig. 23 Received output signal *out*(t)*, 1st derivative pulse *out'(t),* simulated radiated signal $\vec{e}_{\boldsymbol{RAD\_simulated}}(\boldsymbol{\theta} = 90^\circ, \boldsymbol{\varphi} = 0^\circ, \boldsymbol{t})$, measured radiated signal $\vec{e}_{\boldsymbol{RAD\_measured}}(\boldsymbol{\theta} = 90^\circ, \boldsymbol{\varphi} = 0^\circ, \boldsymbol{t})$, normalised power spectrum density

Hence the incident radiated pulse $\vec{e}_{RAD}(\theta, \varphi, t)$ at the receiving antenna can be deduced by using Eq.11

$$\vec{e}_{RAD}(\theta, \varphi, t) = \vec{h}_{RX}(t) \,\overline{*}\, \left[IFFT\left(\vec{S}_{21}(\theta, \varphi, \omega)\right)\right] \tag{11}$$

where the symbol stands for the deconvolution. Using this method, the measured radiated pulse from the transmitting antenna can be compared with the simulated radiated field captured from the virtual probe in the simulation model. It is seen that the measured radiated signal $\vec{e}_{RAD\_measured}(\theta = 90^\circ, \varphi = 0^\circ, t)$ is in good agreement with the simulated radiated signal $\vec{e}_{RAD\_simulated}(\theta = 90^\circ, \varphi = 0^\circ, t)$ as seen in Fig. 22. Figure 23 demonstrates that the signal $\vec{E}_{RAD\_measured}(\theta = 90^\circ, \varphi = 0^\circ, f)$ energy distribution shares similarities, in the UWB frequency range, with the energy spectrum of the $\vec{E}_{RAD\_simulated}(\theta = 90^\circ, \varphi = 0^\circ, f)$ and the 1st order derivative of the reference signal *out'(f)*,

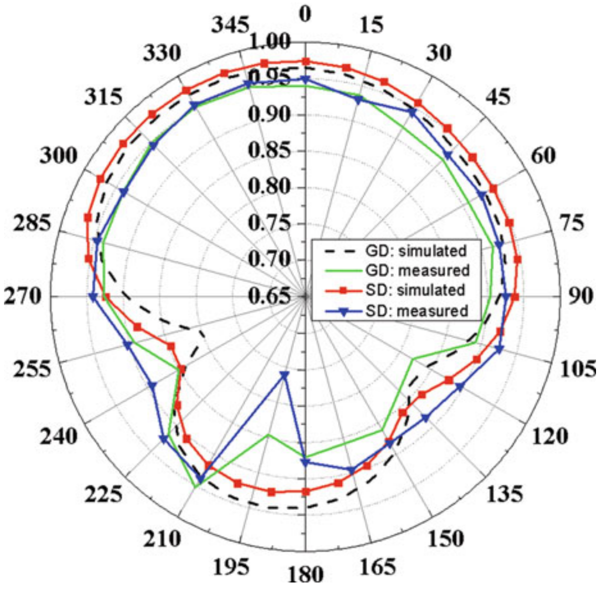

Fig. 24 Measured and simulated FF for an antenna system for Dipole GD and Dipole SD with an equalized modulated SRRC excitation pulse

demonstrating that the transmitting antenna tends to radiate a signal that is approximately proportional to the reference signal derivative at $\theta = 90°$, $\varphi = 0°$.

The transmitting antenna was rotated through 15° angle steps in the radiation plane. The oscilloscope was set to 64-sweep averaging to mitigate spurious sampling artefacts in the measured waveforms. Separate equalization eliminated the dispersive effects due to the cables between the reference antenna and the oscilloscope. The resultant measurement data for the antenna under test was then equivalent to the simulated field-probe data.

The FF was computed by correlating the post-processed received pulse waveforms with the 1st order derivative of the AWG output pulse out'(t). Figure 24 shows the measured FF polar plot for Dipole GD and Dipole SD alongside the simulated results from a modulated SRRC excitation pulse. Good agreement between simulation and measurement is achieved. Furthermore, the measurements validate that an antenna optimized for the full SRRC UWB pulse (Dipole SD) has better time-domain performance for the full UWB range than an antenna optimized with a pulse that does not fit to the FCC UWB spectral mask (Dipole GD).

UWB Localization and Tracking Applications

Impulse Radio UWB (IR-UWB) technology addresses one of the most topical frontiers of emerging wireless communication: precise indoor location and tracking. It allows both accurate measurement of time and data communications to occur simultaneously and so enable a wide variety of applications by developers of real-time location and indoor positioning systems, location-based services, Internet of Things and Wireless Sensor Networks. In healthcare applications doctors and equipment can be located to within centimetres, or children and elderly people can be monitored for their safety and security. In the automotive sector motorists can open and start their cars by simply approaching them. Defence and security can take advantage of weapons that are programmed to respond only to the licensed holder, and military personnel in the field can be tracked. IR-UWB radio devices are currently commercialised (DecaWave, TimeDomain, Zebra Technologies to cite a few) and overcome the intrinsic problems of

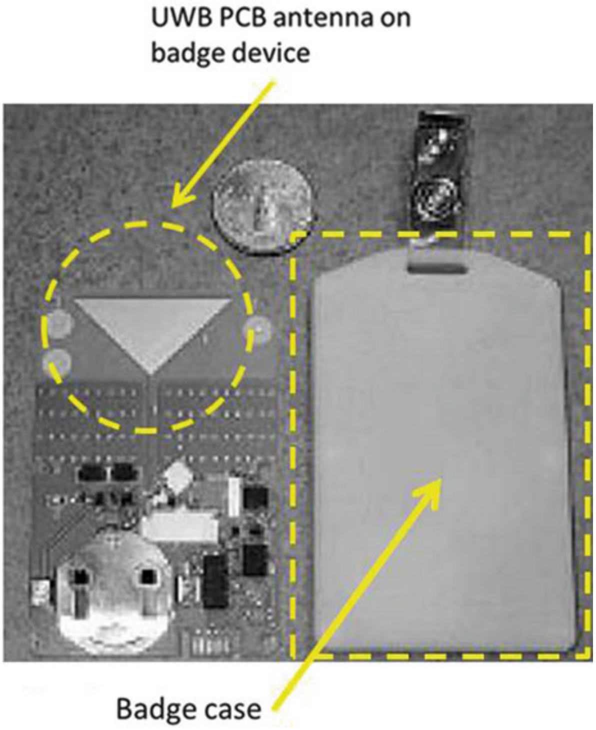

Fig. 25 Tag for IR-UWB personnel tracking (Zebra Technologies DartTag Badge device)

narrowband radio schemes such as high power consumption and poor performance in multipath environments. IR-UWB technology allows longer battery operation and it also enables higher degrees of flexibility in the deployment of wireless networks and sensor positioning, together with increased communication reliability.

Real Time Location Systems are used to track and identify asset tags in real time generally using simple, inexpensive nodes (i.e., badges or tags) attached to or embedded in assets. These tags transmit wireless signals to devices called anchors or readers which employ the wireless signals to determine their location. Current commercial products provide a precision of 10 cm at a distance of up to 300 m in Line-of-Sight (LOS) mode even when devices are moving at speed. High node density is also supported with the accurate location of up to 11,000 items to such precision in a 20 m radius.

Dedicated antenna design is required to deliver this performance. On the tag side, omni-directionality and high compactness are desirable together with pulse fidelity and performance resilience in diverse operating configurations (i.e., close to human body or attached to different materials). But also easy antenna integration on the tag PCB is a required characteristic enabling further miniaturization. Monopole and dipole antennas are a convenient compromise in terms of operating bandwidth, omnidirectional radiation pattern and compactness when integrated on PCB.

In Fig. 25 a commercial product from Zebra Technologies Ltd. for personnel tracking is shown (Online http://www.zebra.com/us/en/products-services/location-solutions/dart-uwb/dart-tag.html). By printing the triangular monopole on the PCB, good compactness and cost reduction are achieved. The tag is approximately the size of a credit card (ID-1 format, 85.60 × 53.98 mm).

Figure 26 shows a tag where a ceramic UWB antenna is integrated on the PCB with the chip. The chip itself together with the metallized board acts as ground for the bevelled monopole (Online http://www.decawave.com/products/dwm1000-module).

While larger antenna solutions are afforded on the anchor device, the requirement for high gain and minimum group delay variation across frequency and angular beamwidth makes the design very

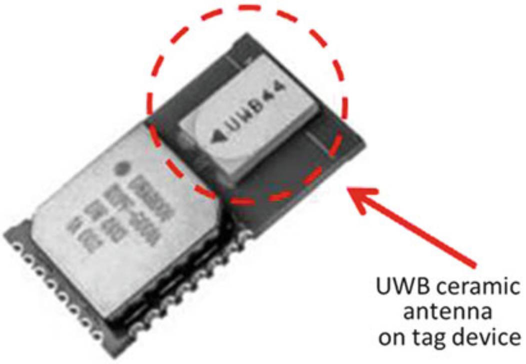

Fig. 26 Tag for IR-UWB radio localization and tracking (DecaWave DWM1000 Module)

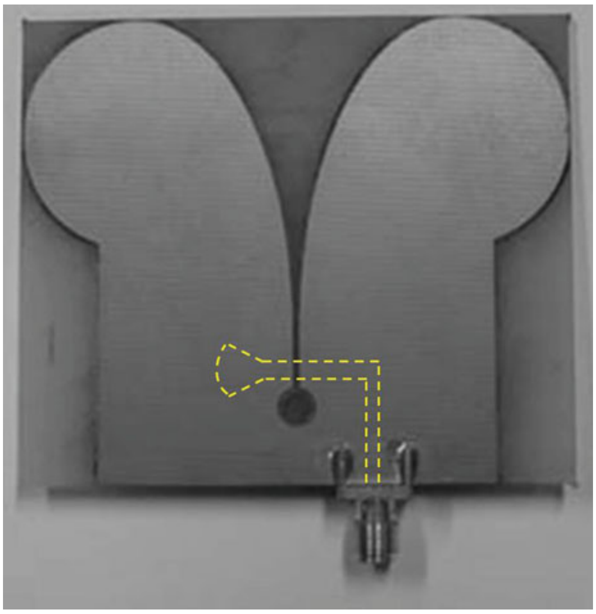

Fig. 27 Modified Vivaldi antenna developed at Queen Mary, University of London

challenging. More directive antennas at the anchor station enable the coverage of larger operating areas. Printed Vivaldi antennas are good candidate for this application due to their large operating bandwidth and directivity.

This antenna with an exponentially tapered slot enables a good trade-off between bandwidth and minimal length. Figure 27 shows a variation of a printed Vivaldi antenna, developed at Queen Mary College, University of London (Valderas et al. 2011). The edge of both arms was rounded to further improve the bandwidth and minimize distortion from the arm-extremities. The antenna is fed through a microstrip to a slot line transformer. The direction of maximum radiation in the Vivaldi antenna corresponds to the aperture between the two arms. In order to reduce the total length of printed tapered slot antennas, variations in the arm profiles were proposed. For instance, the bunny ear antenna (Fig. 28) combines an exponentially tapered aperture with a slot line which is designed to match the 50 Ω input impedance. The element is symmetrically printed on both sides of the substrate and can be easily integrated into a dual-polarized antenna with two centrally intersected PCB slabs (Lee and Livingston 1993).

Fig. 28 Bunny-ear antenna

In their stand-alone conventional configuration, dipole antennas have omnidirectional radiation patterns in the H-plane. The presence of a reflector restricts the operating frequency range of the antenna as it must be placed at a quarter-wavelength distance from the dipole. However, several reported dipole-based antennas have been recently proposed to combine UWB performance, low-profile design and directional radiation patterns (Fig. 29). Examples of band enhancement techniques include the integration of composite reflectors such as E- and H-type corrugated reflectors to support surface currents across a large frequency range (Wu et al. 2010) and minimize destructive current images. In (Wang et al. 2012) a reversed T-match dipole with a flat ground plane was introduced achieving a 77 % operating bandwidth. Small variation input impedance, large bandwidth and stable radiation patterns were reported in (Qu et al. 2009) using a cavity-backed folded triangular bowtie antenna with a rimmed circular reflector.

Circularly Polarized (CP) antennas have been used in a number of radar, communication and navigation systems for many years to mitigate polarization mismatch and reduce orientation constraints between the transmitting and receiving antennas. Recently, systems capable of transmitting and receiving circularly polarized UWB waves were proposed for accurate radio-localization. The objective is to combine the natural immunity of CP transmit/receive systems to arbitrary polarisation alignment with high spatial and temporal resolutions provided by UWB short pulse signals (Shlivinski 2009). But this creates two significant challenges for the antenna engineer: increasing circular polarization across a large operating bandwidth while satisfactory time-domain performance is provided. In Qing et al. (2007) use a three-stub hybrid coupler to provide controlled power division to two orthogonal UWB slot antennas over the frequency range 2.8–5.2 GHz, shown in Fig 30.

The investigation is carried out in terms of typical frequency-domain parameters to characterize CP antennas (i.e., impedance matching, gain, axial ratio, radiation patterns) with further analysis in the time-domain in terms of pulse-distortion, group delay variation and fidelity.

The same operating principle of directing equal signals to two orthogonal UWB antennas is also adopted by Narbudowicz et al. in (2012) but applied to directive antipodal Vivaldi antennas. The input signal is split using a 3-stage Wilkinson divider to provide smooth transmission with minimal variation between antenna feeds. The desired 90° phase shift between the antenna feeds is obtained in two stages by

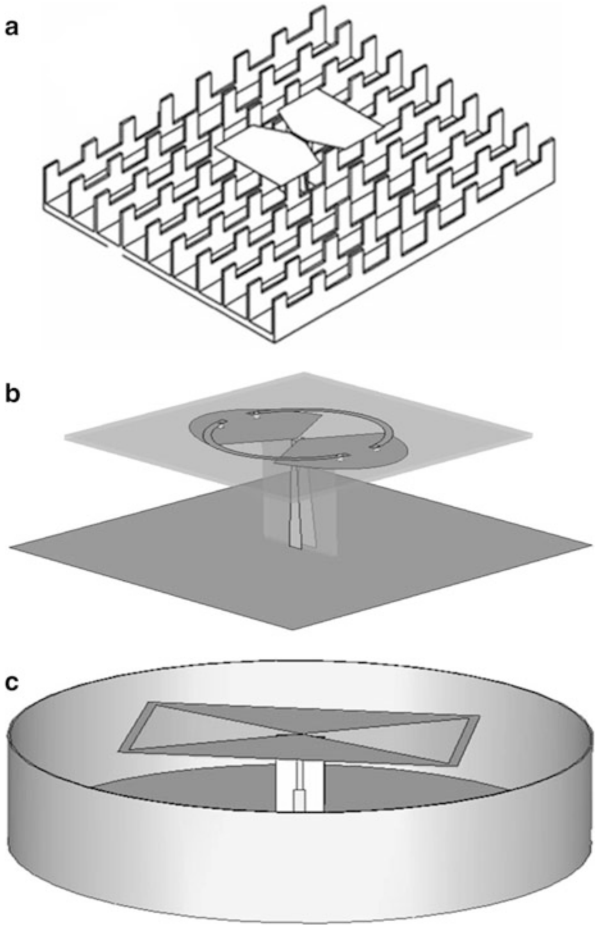

Fig. 29 Bandwidth enhancement techniques for directive dipole antennas. (a) E- and H-type corrugated reflector; (b) Reversed T-match dipole; (c) cavity-backed folded triangular bowtie antenna

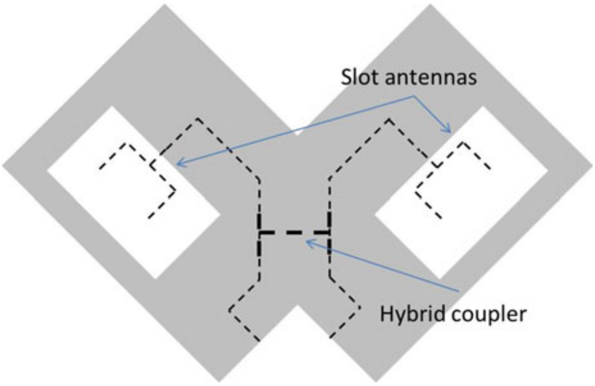

Fig. 30 Ultra-wideband Circularly Polarized Wide-slot Antenna Fed by Three-stub Hybrid Coupler

coupling the signal through the elliptical slot in the ground plane to a microstip line located on the rear side of the dielectric (Fig. 31). Although the mismatch of the two phase centers generates a small tilt in the main beam, this can be mitigated by placing the antennas as close as possible.

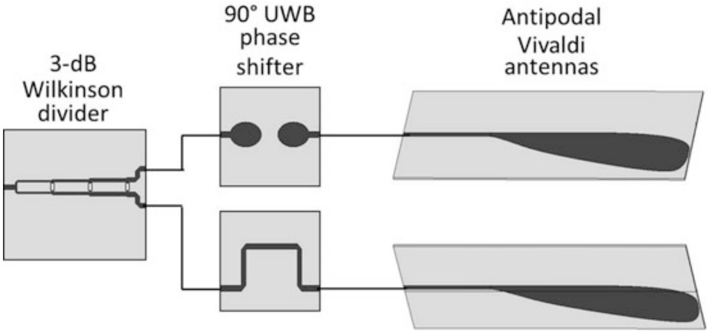

Fig. 31 Vivaldi array for generation of directional UWB circular polarization

Biomedical UWB Imaging

Microwaves and millimeter waves have been widely used as a successful and low-cost imaging method for dielectric structures. In this spectrum, electromagnetic waves have wavelengths ranging from a millimeter to a meter and can penetrate into several optically opaque media. In particular, when UWB radar technology is used, target detection can be achieved with high accuracy. Compared to narrowband systems, UWB radar offers greater imaging resolution and improved target characterization. Recently, UWB radar technology has been successfully proposed in biomedical diagnostics.

UWB microwave imaging techniques for biomedical scenarios are based on the transmission of low-power short microwave pulses (tens picoseconds to nanoseconds) into the body and the consequent detection of the differentiated scattering due to the dielectric contrast between the target and healthy tissues. The advantage of using short pulses is due to easier identification of the target contribution in the received scattered signal. This consists of the incident signal together with a large number of delayed and attenuated replicas from dielectric discontinuities inside human tissue. Narrowband antennas would generate larger pulses and overlapping signal replicas which can hide the informative signals coming from the target. The short pulses are advantageous in detecting a target in human tissue, but the UWB antenna design presents several challenges.

Human tissue such as skin, muscle, fat, brain, and many others present very different electrical properties from those of air. Starting with the skin layer with a relative permittivity around 30 and a specific conductivity of about 3 S/m in the low GHz range, deeper layers of fat, muscle, fibro-glandular and connective tissues contribute to the rejection of the microwave power due to reflection and dissipation. Moreover, the electrical properties of tissue exhibit strong dispersion with frequency in the RF and microwave spectra. In this difficult propagation scenario the electromagnetic signal is subjected to strong attenuation and distortion. Moreover, the attenuation between incident and penetrated signal challenges the dynamic range of the measurement setup and the UWB signal distortion can make the imaging formation process extremely difficult, resulting in clutter which masks the signal scattered by the target. The attenuation and distortion limitations tolerable by the imaging system translate into the following requirements for a successful diagnostic procedure:

- The system must provide appropriate penetration into the body area under assessment;
- The coupling mechanism between sources, sensors and the body must be stable across the operating bandwidth and screening configurations.

The design of the UWB antenna plays a vital role. The first consideration comes from the strong rejection of electromagnetic signals by skin and deeper layers for frequencies above 10 GHz. A few centimeters of tissue along the direction of propagation can attenuate a 10 GHz signal by more than 80 dB. Good signal penetration can be achieved at lower frequencies (i.e., below 1 GHz). However, the allocation of the operating bandwidth is compromised by the requirement for compact antennas. The diagnostic device design involves the integration of small antennas to facilitate manoeuvrability or array integration. Size reduction is often achieved by immersing the antenna into a liquid solution with a dielectric constant similar to that of tissue. This medium provides an impedance transformation between the antenna and the body, improving tissue coupling.

Another important constraint for the designer is to provide resilience of antenna performance under all operating configurations. In particular, adequate impedance matching must be maintained with the antenna in close proximity to different body areas and for different antenna-skin separation. Suitable antenna designs should be capable of screening interference by backscatter from undesired directions.

Frequency-domain characterization of antennas is not appropriate for biomedical imaging applications where near-field conditions occur. Parameters such as gain, radiation efficiency, phase center and radiation pattern refer to far-field conditions and are not suitable in scenarios where the body strongly couples to reactive fields. These parameters rapidly change when the antenna is in close proximity to the body as in typical medical imaging configurations. The dramatic dependence of the antenna behaviour on scanning position and the body area necessitates alternative quality figures. This is validated by numerical tools which simulate the complex electromagnetic problems in the presence of highly detailed voxel models which reproduce the morphology and the electrical dispersion of benign and malignant tissues. But tissue-mimicking phantoms can also enable ad-hoc antenna characterization at the experimental stage.

Although in realistic scenarios tissue morphology changes from patient to patient with consequent variations in antenna response, specific parameters of merit were introduced to characterize antennas in biomedical imaging applications. For this purpose, standard testing configurations were proposed to combine the requirement of approximating a realistic operating situation in a controlled environment (Fig. 32). The following parameters are able to characterize the antenna in terms of properties which are useful for a near-field UWB radar imaging application.

Fidelity Factor: calculated as the maximum magnitude of the cross correlation between the normalized transmitted and the normalized received response across tissue-mimicking multi-layer structures.

Pulse duration: For radar-based breast cancer detection it is important that pulses produced by the antenna are as short as possible with minimal late-time ringing (Gibbins et al. 2010). Therefore pulse duration is a good indication of the ability of the antenna to effectively transmit UWB signals into the medium. The time taken for 99 % of the energy of these pulses to be received can be calculated for different antenna polarizations and across a defined angular beamwidth.

Half Energy Beam (HEB) and *Half Energy Beamwidth (HEBW)*: The HEB and HEBW are based on the Energy Flux Density (EFD) which is calculated by summing time samples of the instantaneous Poynting vector over the duration of the simulation time (Bourqui et al. 2010). In the near-field, the HEB is defined on a plane which is orthogonal to the main radiation beam and situated at a given distance from the antenna aperture as shown in Fig. 33. The HEB describes the region over which the energy is greater than half of the maximum value on the selected plane. Accordingly, the HEBW is defined by the angular width of this region.

Among different screening typologies under investigation, breast cancer imaging has advanced faster and is currently at a clinical trial stages. Hagness et al. pioneered this imaging modality by proposing small UWB microwave radar systems to detect malignant tumors in the breast (Hagness et al. 1998). Encouraging outcomes and the critical necessity for developing early-stage breast cancer screening tools with high sensitivity and specificity prompted significant research efforts which have grown into a well-established microwave application (Hagness et al. 2012). Microwave imaging of breast cancer is either

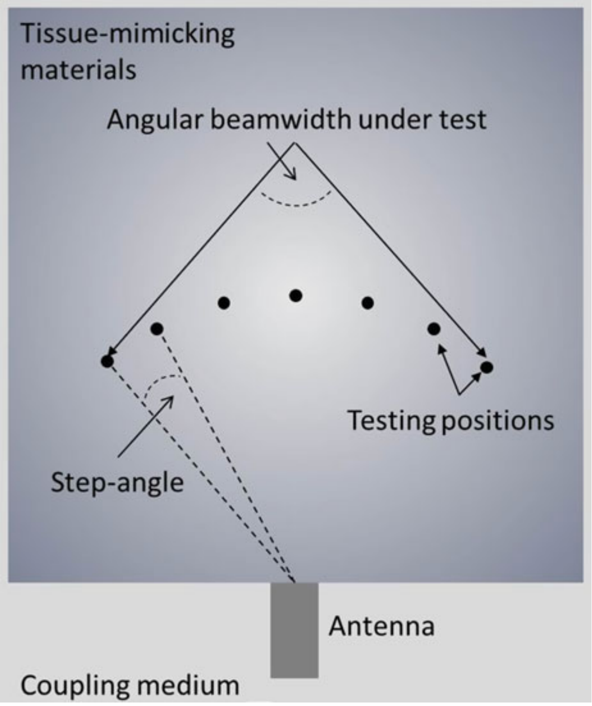

Fig. 32 Testing configuration for imaging-specific parameters

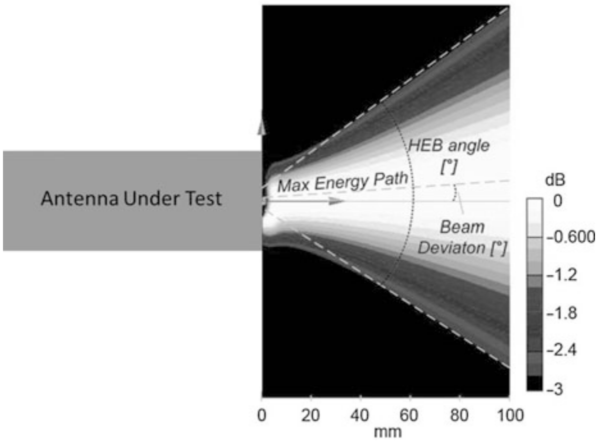

Fig. 33 Half energy area in one plane and HEB representation

based on mapping the permittivity and conductivity distributions as functions of position or the simple detection of malignant tissues. With both approaches measured data are collected by antennas in specific positions and then processed in search of scatterers, i.e., objects with properties which differ from those in the normal or healthy state of the imaged body region. Accordingly, the more electrically similar a tumor is to its surrounding benign tissues, the more challenging it is to detect it. The dielectric contrast between malignant and benign tissues is generally defined as the ratio, often in percentage, of the permittivities (or the conductivities) of the scatterer and the host medium. Recent studies (Sha et al. 2002; Lazebnik et al. 2007a, b; Meaney et al. 2007; Poplack et al. 2007; Halter et al. 2009) indicate that while contrasts

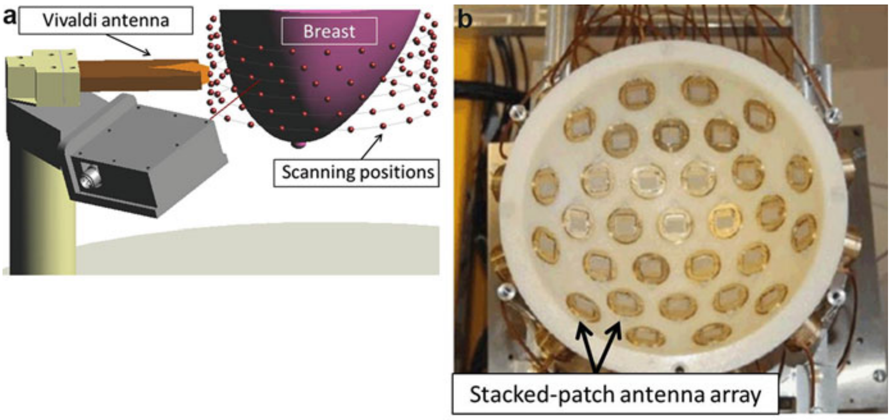

Fig. 34 Breast cancer imaging systems. (**a**) Monostatic scanner at the University of Calgary, Canada; (**b**) Multistatic scanner at the University of Bristol, UK

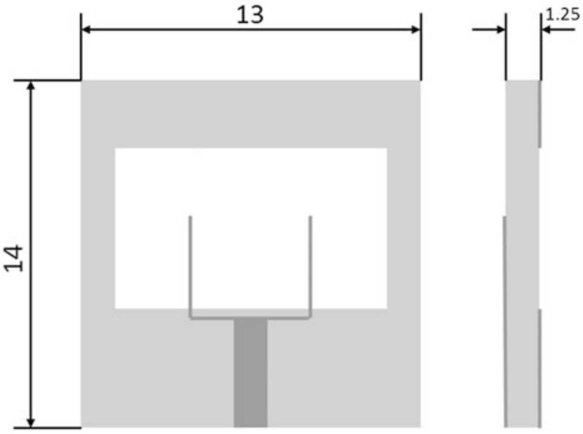

Fig. 35 Geometry of the wide-slot antenna developed at the University of Bristol. All dimensions are in mm

between malignant and adipose breast tissue may be as large as 10, those between malignant and healthy fibroglandular tissues can be as low as 1.1 in both permittivity and conductivity.

Both mono- and multi-static radar architectures have been proposed for microwave breast cancer imaging (Fig. 34). Whether the antenna is a fixed array element displaced around the body area or the antenna moves across different screening positions, its performance must be stable for all configurations.

Numerous antenna designs for radar-based UWB microwave breast imaging have been proposed over the past 15 years. A wide slot antenna with interesting features for UWB cancer detection was developed at the University of Bristol (Gibbins et al. 2010) (Fig. 35). This antenna is surface-mounted on a hemispherical bowl to form a 31-element array and function as a multi-static system with 465 independent measurements (Klemm et al. 2011). The imaging system operates in the full UWB frequency range, between 3 and 10 GHz. Both these antennas mainly consist of printed dielectric substrates with a relative permittivity of 10.2. The geometry was optimized to operate with the antenna face immersed in a matching medium with dielectric properties that mimics that of human breast tissue, in order to reduce reflections by eliminating the air/skin interface (Sill and Fear 2005). The matching medium used is mainly a solution made of paraffin oil and distilled water. This mixture has a relative permittivity of between 9 and 10 in the 2–10 GHz region and an attenuation of 2 dB/cm at 8 GHz. The wide-slot antenna developed at

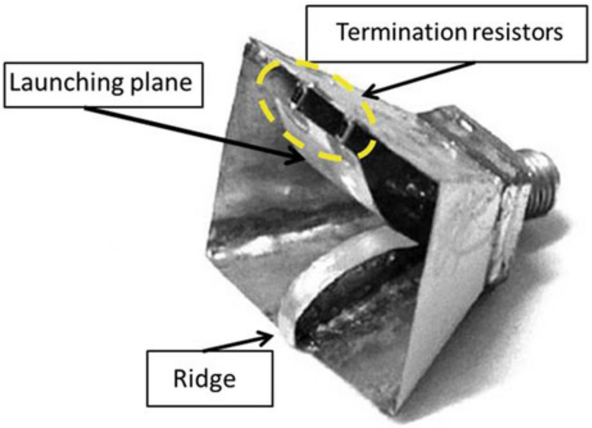

Fig. 36 Modified ridged pyramidal horn antenna with curved launching plane developed at the University of Wisconsin

the University of Bristol consists of an approximately square slot cut out from a ground plane which is printed on one side of a substrate with relative permittivity of 10.2. The slot is fed by a forked microstrip feed that splits just below the slot from a 50 Ω feed into two 100 Ω sections. The fork feed excites multiple resonances with a consequent increase of the impedance matching bandwidth.

A cavity is attached to the antenna on the side where the microstrip feed is located. This small cavity prevents any radiation from the antenna rear side (opposite to skin interface) coupling with other elements in the array. The cavity is absorber lined and also stops interference from spurious radiation on the imaging formation process. The antenna provides suitable bandwidth for use in UWB detection systems. In consideration of the complex array architecture where the antenna operates, inter-element transmission properties were also investigated. The wide-slot antenna presents a stable transfer function over a large angular range across bore-sight direction. This results in a fidelity factor better than 90 % for angles up to 60° from boresight and reduced late-time ringing and distortion of transmitted signals.

For monostatic data collection more voluminous three-dimensional antenna designs may be suitable. A ridged pyramidal horn antenna (Li et al. 2003) was reported by the University of Wisconsin, and resistively loaded dipole, tapered slot, transverse electromagnetic horn, and balanced antipodal Vivaldi antennas have been presented by the University of Calgary (Bourqui et al. 2009). Li et al. proposed a modified ridged pyramidal horn antenna with a curved launching plane (Fig. 36). The bandwidth of horn antennas can be increased significantly by adding metallic ridges to the waveguide and flared sections (Walton and Sundberg 1964). In Li's antenna one of the two ridges is replaced by a curved metallic plane terminated by two 100-Ω resistors that suppress reflections from the end of the launching plane (Fig. 36). The waveguide section was eliminated to reduce size. The pyramidal horn has a depth of 13 mm with a 25 mm × 20 mm aperture and is connected to the outer conductor of the coaxial feed and serves as the ground plane, providing a current return path. The maximum width of the tapered launching plane is 12 mm, whereas the thickness of the ridge is 2 mm. The antenna is made of brass and fed by an SMA connector. Thickness, curvature and shape of the launching plane critically control the input impedance of the antenna. But its tapered profile prevents reflections which can distort the pulse.

In 2010 Bourqui et al. proposed a modified balanced antipodal Vivaldi antenna (BAVA) which includes a profiled high dielectric section placed in the antenna aperture (Bourqui et al. 2010). The BAVA provides a more compact profile combined with near-field focusing of the energy in the endfire direction. This antenna was designed to operate in a monostatic scanner immersed in canola oil. From 1 to 14 GHz, the permittivity and conductivity of this coupling medium varies from 2.55 to 2.35 and 0.01–0.04 S/m, respectively. The antenna consists of three copper layers; the two external layers are the ground planes and the central layer is the conductor (Fig. 37). The copper layers are printed on two dielectric substrates

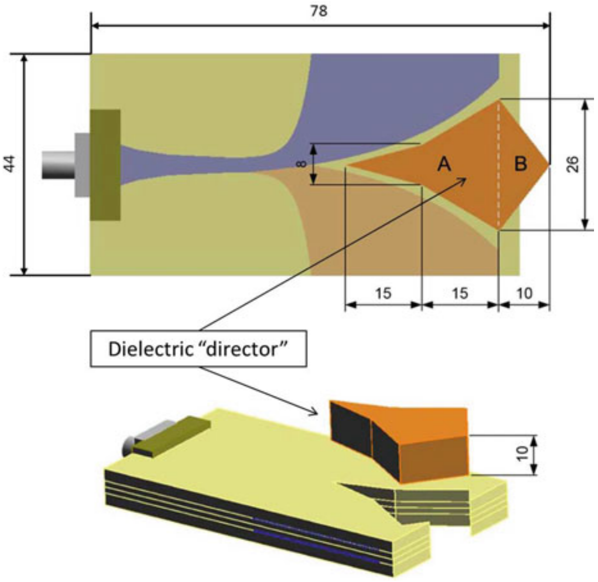

Fig. 37 BAVA including a higher dielectric permittivity director developed at the University of Calgary. All dimensions are in mm

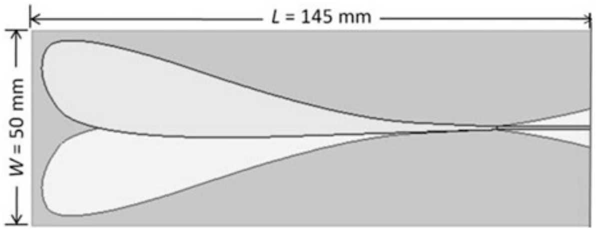

Fig. 38 ParEGO optimized antipodal Vivaldi antenna developed at the Antenna & High Frequency Research Centre, Dublin Institute of Technology, Ireland. All dimensions are in mm

(supportive substrates) and two additional dielectric layers are stacked on each side of the antenna (stacking substrates) to balance the dielectric loading between the conductor and ground planes. As a result of this solution, the usual beam squint observed across frequency in this type of antenna (Langley et al. 1996) is considerably reduced. Moreover, for this application, the energy coupling is improved since contact between the lossy canola oil and the external copper layer is avoided. The director is made of Eccostock HIK material with a relative permittivity of 6. The shape of the director is designed to prevent reflections from its extremities and to enhance near-field focusing. The effect of such narrower beamwidth was verified with the transmitted energy between two antennas being significantly greater in the presence of the director. Furthermore, it was demonstrated that the presence of the director in the aperture of the BAVA increases the backscatter energy from an object placed in front of the antenna, such as a tumor embedded in the breast.

Selective illumination of the breast may assist in tumor localization. In the context of microwave imaging applications, a more focused beam illuminates a smaller volume which can increase the tumor-to-clutter ratio. Ruvio et al. compared three antennas with different coupling mechanisms and focusing capability for a UWB mono-static radar illumination of a tumor embedded in a 2-D multi-layer breast-mimicking phantom (Ruvio et al. 2014). In particular, an antipodal Vivaldi antenna shown in Fig. 38 was optimized by means of a ParEGO algorithm to provide a stable transfer function over the operating bandwidth ranging from 1 to 3 GHz when immersed in a coupling medium with permittivity of 12. Both numerical and experimental results show the antipodal Vivaldi antenna outperforms a coplanar and a semi-folded monopole as it enables more pronounced clutter mitigation in reconstructions.

Future Directions and Open Problems

The main research activity on UWB antennas is currently driven by emerging applications in biomedicine and security. Since UWB imaging provides low-cost, high resolution imaging, good target recognition and robust immunity to passive jamming, it has the potential to replace or complement the ionizing radiation used in conventional non-invasive imaging applications. Emerging biomedical applications include UWB microwave impedance spectroscopy (non-invasive measurement of glucose and cholesterol levels in blood) and vital signs detection. Security applications include a low-cost alternative detection of concealed metal objects, as well as through-the-wall imaging, body-area networks and asset-tracking. Automotive applications include vehicle entry systems and relay attack avoidance. In the agricultural sector, livestock tracking and feed control methods using UWB are evolving.

Some of the main challenges facing UWB antenna design relate to the environment. For example, close proximity to the body realises dielectric loading which is highly sensitive to proximity distance. There is demand for antennas which are resilient to this loading across all applications. New parameters are required to describe UWB antennas when in close proximity with media which are not known a priori (on-body networks, ground penetrating radar, through-the-wall imaging, microwave breast cancer imaging. . .). These parameters would describe antenna resilience to proximity of these media.

In communications applications, UWB antennas may also be employed in multi-band or cognitive radio applications. Of course, UWB antennas are not confined to 3.1–10.6 GHz with activity below (ground penetrating radar) and above this band. High rate communications in the 57–66 GHz band is the focus of research on UWB antennas on-chip packaging (→On-chip Antennas).

Cross-References

- ▶ Broadband and Multiband Planar Antennas
- ▶ Low-profile Antennas
- ▶ Omni-directional Antennas
- ▶ On-chip Antennas
- ▶ Optimization Methods in Antenna Engineering

References

Agrawall NP, Kumar G, Ray KP (1998) Wide-band planar monopole antenna. IEEE Trans Antennas Propag 46(2):294–295

Allen B, Dohler B, Okon EE, Malik WQ, Brown AK, Edwards JD (2007) Introductions to UWB signals and systems. In: Ultra-wideband antennas and propagation for communication radar and imaging. Wiley, Chichester

Ammann MJ (1999) Square planar monopole antenna. IEE National Conference on Antennas and Propagation:37–40

Ammann MJ (2001) Control of the impedance bandwidth of wideband planar monopole antennas using a bevelling technique. Microw Opt Technol Lett 30(4):229–232

Ammann MJ, Chen ZN (2003a) A wideband shorted planar monopole with bevel. IEEE Trans Antennas Propag 51(4):901–903

Ammann MJ, Chen ZN (2003b) Wideband monopole antennas for multiband wireless systems. IEEE Antennas Propag Mag 45(2):146–150

Angelopoulos ES, Anastopoulos AZ, Kaklamani DI, Alexandridis AA, Lazarakis F, Dangakis K (2006) Circular and elliptical CPW-fed slot and microstrip-fed antennas for ultrawideband applications. IEEE Antennas Wirel Propag Lett 5:294–297

Azevedo S, McEwan TE (1996) Micropower impulse radar. Science & Technology Review: 17–29

Balanis CA (2005) Historical advancement. In: Antenna theory, analysis and design, Thirdth edn. Wiley, Hoboken, p 20

Barret TW (2001) History of ultra wideband communication and radar: part I, UWB. Microw J 44(1):22–54

Bartels RH, Beatty JC, Barsky BA (1996) An introduction to splines for use in computer graphics and geometric modeling. Morgan Kaufmann, Burlington

Bourqui J, Campbell MA, Sill J, Shenouda M, Fear EC (2009) Antenna performance for ultra-wideband microwave imaging. In: IEEE Radio Wireless Symposium, San Diego, US, pp 522–525

Bourqui J, Okoniewski M, Fear EC (2010) Balanced antipodal Vivaldi antenna with dielectric director for near-field microwave imaging. IEEE Trans Antennas Propag 58(7):2318–2326

Cerny P, Mazanek M (2007) Optimization of transient response radiation of printed ultra wideband dipole antennas. Radioengineering 16(2):1–6

Chamaani S, Mirtaheri SA, Abrishamian MS (2011) Improvement of time frequency-domain performance of antipodal Vivaldi antenna using multiobjective particle swarm optimization. IEEE Trans Antennas Propag 59(5):1738–1742

Chen HD, Li JN, Hung YF (2006a) Band-notched ultra-wideband square slot antenna. Microw Opt Technol Lett 48(12):2427–2429

Chen X (2007) Theory of UWB antenna elements. In: Allen B, Dohler B, Okon EE, Malik WQ, Brown AK, Edwards JD (eds) Ultra-wideband antennas and propagation for communications, radar and imaging. Wiley, Chichester, pp 111–145

Chen ZN (2000) Impedance characteristics of planar bow-tie-like monopole antennas. Electron Lett 36(13):1100–1101

Chen ZN, Ammann MJ, Qing XM, Wu XH, See TSP, Cai A (2006b) Planar antennas: promising solutions for microwave UWB applications. Microw Mag 7(6):63–73

Chen ZN, Qing X, Chia MYW (2005) UWB characteristics of disc cone antenna. In: IEEE international workshop on antennas technology, Singapore, pp 97–100

Chen ZN, Wu XH, Li HF, Yang N, Chia MYW (2004) Considerations for source pulses and antennas in UWB radio systems. IEEE Trans Antennas Propag 52(7):1739–1748

Donelli M, Massa A (2005) Computational approach based on a particle swarm optimizer for microwave imaging of two-dimensional dielectric scatterers. IEEE Trans Microwave Theory Tech 53(5):1761–1776

Dubost G, Zisler S (1976) Antennes à large bande. Masson, Paris/New York, pp 128–129

Dumoulin A, John M, Ammann MJ, McEvoy P (2012) Optimized monopole and dipole antennas for UWB asset tag location systems. IEEE Trans Antennas Propag 60(6):2896–2904

Duroc Y, Ghiotto A, Vuong TP, Tedjini S (2007) UWB Antennas: systems with transfer function and impulse response. IEEE Trans Antennas Propag 55(5):1449–1451

Evans JA, Ammann MJ (1999) Planar trapezoidal and pentagonal monopoles with impedance bandwidths in excess of 10:1. In: IEEE international symposium on antennas and propagation, vol 3, Orlando, FL, USA, pp 1558–1561

Foley JD, van Dam A, Feiner SK, Hughes JF, Phillips RL (1993) Introduction to computer graphics. Addison-Wesley, Reading

Ghosh D, De A, Taylor MC, Sarkar TK, Wicks MC, Mokole EL (2006) Transmission and reception by Ultra-Wideband (UWB) antennas. IEEE Antennas Propag Mag 48(5):67–99

Gibbins D, Klemm M, Craddock IJ, Leendertz JA, Preece A, Benjamin R (2010) A comparison of a wide-slot and a stacked patch antenna for the purpose of breast cancer detection. IEEE Trans Antennas Propag 58(3):665–674

Go HC, Jung YW (2004) Multi-band modified fork-shaped microstrip monopole antenna with ground plane including dual-triangle portion. Electron Lett 40(10):575–577

Griffiths LA, Fuse C, Chung YC (2005) BroadBand and multiband antenna design using the genetic algorithm to create amorphous shapes using ellipses. IEEE Trans Antennas Propag 54(10):2776–2782

Guo L, Liang J, Chiau CC, Chen X, Parini CG, Yu J (2007) Performance of UWB disc monopoles in time-domain. Microw Antennas Propag 1(4):955–959

Hagness SC, Fear EC, Massa A (2012) Guest editorial: special cluster on microwave medical imaging. IEEE Antennas Wirel Propag Lett 11:1592–1597

Hagness SC, Taflove A, Bridges JE (1998) Two-dimensional FDTD analysis of a pulsed microwave confocal system for breast cancer detection: fixed-focus and antenna-array s. IEEE Trans Biomed Eng 45:1470–1479

Halter RJ, Zhou T, Meaney PM, Hartov A, Barth RJ, Rosenkranz KM, Wells WA, Kogel CA, Borsic A, Rizzo EJ, Paulsen KD (2009) The correlation of in vivo and ex vivo tissue dielectric properties to validate electromagnetic breast imaging: initial clinical experience. Physiol Meas 30(6):121–136

Hammoud M, Poey P, Colombel F (1993) Matching the input impedance of a broadband disc monopole. Electron Lett 29(4):406–407

Haupt RL (2007) Antenna design with a mixed integer genetic algorithm. IEEE Trans Antennas Propag 55(3):577–582

Honda S, Ito M, Seki H, Jinbo Y (1991) On a broadband disk monopole antenna. Technical Report of Television Society Japan. ROFT 91–55

Honda S, Ito M, Seki H, Jinbo Y (1992) A disk monopole antenna with 1:8 impedance bandwidth and omnidirectional radiation pattern. In: ISAP'92, Sapporo, pp 1145–1148

http://www.decawave.com/products/dwm1000-module

http://www.zebra.com/us/en/products-services/location-solutions/dart-uwb/dart-tag.html

IEEE Computer Society (2011) Part 15.4: low-rate wireless personal area networks (LR-WPANS). IEEE, New York

IEEE Standard 802.15.4a (2007) Part 15.4: wireless medium access control (MAC) and Physical Layer (PHY) Specifications for Low-Rate Wireless Personal Area Networks (WPANs)

Jin N, Rahmat-Samii Y (2005) Parallel particle swarm optimization and finite- difference time-domain (PSO/FDTD) algorithm for multiband and wide-band patch antenna designs. IEEE Trans Antennas Propag 53(11):3459–3468

John M, Ammann MJ (2007) Wideband printed monopole design using a genetic algorithm. IEEE Antennas Wirel Propag Lett 6:447–449

John M, Ammann MJ (2009) Antenna optimisation with a computationally efficient multiobjective evolutionary algorithm. IEEE Trans Antennas Propag 57(1):260–263

Johnson JM, Rahmat-Samii Y (1997) Genetic algorithms in engineering electromagnetic. IEEE Antennas Propag Mag 39(4):7–21

Kanda M (1986) Time-domain sensors and radiators. In: Miller EK (ed) Time-domain measurements in electromagnetic. Van Nostrand Reinhold, New York, p 125

Karacolak T, Topsakal E (2006) A double-sided rounded bow-tie antenna (DSRBA) for UWB communications. IEEE Antennas Wirel Propag Lett 5:446–449

Klemm M, Fumeaux C, Baumann D, Craddock IJ (2011) Time-domain simulations of a 31-antenna array for breast cancer imaging. In: IEEE international symposium on antennas and propagation, Spokane, Washington, USA, pp 710–713

Kuo YL, Wong KL (2002) Dual polarised monopole antenna for wireless LAN operation. IEEE Intl. Antennas & Propagat. Symp. Dig. 4:80–83

Kwon HD (2006) Effect of antenna gain and group delay variations on pulse-preserving capabilities of ultrawideband antennas. IEEE Trans Antennas Propag 54(8):2208–2215

Langley J, Hall P, Newham P (1996) Balanced antipodal Vivaldi antenna for wide bandwidth phased arrays. Inst Elect Eng Microwaves Antennas Propag 143(2):97–102

Lazebnik M, McCartney L, Popovic D, Watkins CB, Lindstorm MJ, Harter J, Sewall S, Magliocco A, Brooske JH, Okoniewski M, Hagness SC (2007a) A large-scale study of the ultrawideband microwave dielectric properties of normal breast tissue obtained from reduction surgeries. Phys Med Biol 52(10):2637–2656

Lazebnik M, McCartney L, Popovic D, Watkins CB, Lindstorm MJ, Harter J, Sewall S, Magliocco A, Brooske JH, Okoniewski M, Hagness SC (2007b) A large-scale study of the ultrawideband microwave dielectric properties of normal, benign and malignant breast tissues obtained from cancer surgeries. Phys Med Biol 52(20):6093–6115

Lee JJ, Livingston S (1993) Wide band bunny-ear radiating element. In: IEEE international symposium on antennas and propagation, vol 3, Ann Arbor, US, pp 1604–1607

Li X, Hagness SC, Choi MK, van der Weide D (2003) Numerical and experimental investigation of an ultrawideband ridged pyramidal-horn antenna with curved launching plane for pulse radiation. IEEE Antennas Wirel Propag Lett 2:259–262

Liang J, Chiau CC, Chen X, Parini CG (2004) Printed circular disc monopole antenna for ultra-wideband applications. Electron Lett 40(20):246–1247

Liang J, Chiau CC, Chen X, Parini CG (2005) Study of a printed circular disk monopole antenna for UWB systems. IEEE Trans Antennas Propag 53(11):3500–3504

Lizzi L, Manica L, Massa A (2009) Time-domain analysis for UWB antenna synthesis. In: Proceedingds of the 39th European microwave conference, Rome, pp 93–96

Lizzi L, Oliveri G, Massa A (2012) A time-domain approach to the synthesis of UWB antenna systems. Prog Electromagn Res 122:557–575

Mandke K, Nam H, Yerramneni L, Zuniga C (2003) The evolution of UWB and IEEE 802.15.3a for very high data rate WPAN. [Online]. Available: http://kom.aau.dk/group/03gr993/Papers/802.15/GT3a.pdf. Accessed 21 Aug 2014

Meaney PM, Fanning MW, Raynolds T, Fox CJ, Fang Q, Kogel CA, Poplack SP, Paulsen KD (2007) Initial clinical experience with microwave breast imaging in women with normal mammography. Acad Radiol 14(2):207–218

Meinke H, Gundlach FW (1968) Taschenbuch der Hochfrequenztechnik. Springer, Berlin, New York, pp 531–535

Narbudowicz A, John M, Bao X, Ammann MJ (2012) Vivaldi array for generation of UWB circular polarization. In: IEEE international symposium on antennas and propagation, Chicago, US, pp 1–2

Poplack SP, Tosteson TD, Wells WA, Pogue BW, Meaney PM, Hartov A, Kogel CA, Soho SK, Gibson JJ (2007) Electromagnetic breast imaging: results of a pilot study in women with abnormal mammograms. Radiology 243:350–359

Qing X, Chen ZN, Chung HL (2007) Ultra-wideband circularly polarized wide-slot antenna fed by three-stub hybrid coupler. In: IEEE international conference on ultra-wideband, Singapore, pp 487–490

Qu SW, Li JL, Xue Q, Chan CH, Li S (2009) Wideband and unidirectional cavity-backed folded triangular bowtie antenna. IEEE Trans Antennas Propag 57(4):1259–1263

Rambabu K, Tan AEC, Chan KKM, Chia MYW (2009) Estimation of antenna effect on ultra-wideband pulse shape in transmission and reception. IEEE Trans Electromagn Compat 51(3):604–610

Ruvio G, Solimene R, Cuccaro A, Gaetano D, Browne JE, Ammann MJ (2014) Breast cancer detection using interferometric MUSIC: experimental and numerical assessment. Medical Physics 41(10), 103101/1–11

Schantz HG (2004) Dispersion and UWB antennas. In: Proceedings of the conference on . ultrawideband systems and technologies, conference: Kyoto, Japan

Schantz HG, Fullerton L (2001) The diamond dipole: a Gaussian impulse antenna. In: Proceedings of antennas and propagation society international symposium conference: Boston, MA, USA

Sha L, Ward ER, Story B (2002) A review of dielectric properties of normal and malignant breast tissue. IEEE Southeast conference, Columbia, US, pp 457–462

Shlivinski A (2009) Time-domain circularly polarized antennas. IEEE Trans Antennas Propag 57(6):1606–1611

Sill J, Fear EC (2005) Tissue sensing adaptive radar for breast cancer detection: study of immersion liquids. Electron Lett 41(3):113–115

Siwiak K, McKeown D (2004) Radiation of UWB signals. In: Ultra-wideband radio technology. John Wiley & Sons Ltd, New York, p 111

Telzhensky N, Leviatan Y (2006) Novel method of UWB antenna optimization for specified input signal forms by means of genetic algorithm. IEEE Trans Antennas Propag 54(8):2216–2225

Valderas D, Sancho JI, Puente D, Ling C (2011) Ultrawideband antennas: design and applications. Imperial College Press, London, p 179

Walton KL, Sundberg VC (1964) Broadband ridged horn design. Microw J 4:96–101

Wang S, Wu Q, Su D (2012) A novel reversed T-match antenna with compact size and low profile for ultrawideband applications. IEEE Trans Antennas Propag 60(10):4933–4937

Wu Q, Jin R, Geng J, Su D (2010) On the performance of printed dipole antenna with novel composite corrugated-reflectors for low-profile ultrawideband applications. IEEE Trans Antennas Propag 58(12):3839–3846

Zhang X, Larson LE, Asbeck PM (2003) Design of linear RF outphasing power amplifiers. Artech House Inc, Boston, p 47